Title
Mechanisms of Long-Range Edge Retraction of Au/Ni Bilayer Films

Author
Jamadagni, Bhagyashree

Publication Date
2021

Peer reviewed|Thesis/dissertation

Mechanisms of Long-Range Edge Retraction of Au/Ni Bilayer Films

By

BHAGYASHREE JAMADAGNI

THESIS

Submitted in partial satisfaction of the requirements for the degree of

MASTER OF SCIENCE

in

Materials Science and Engineering

in the

OFFICE OF GRADUATE STUDIES

of the

UNIVERSITY OF CALIFORNIA

DAVIS

Approved:

_____

Klaus van Benthem, Chair

_____

Subhash Risbud

_____

Sabyasachi Sen

Committee in Charge

2021

Acknowledgements

There are many people without whom I would not be where I am today and so, I would like to recognize and thank them sincerely for the support they have given me throughout this journey. First and foremost, I would like to express my sincere gratitude to my mentor, Dr. Klaus van Benthem, for his support and his guidance, both in academics and in life. His shrewdness as a researcher and his kindness as a person have been invaluable to me and were the reasons for why I wanted to be part of his group when I started as a student at UC Davis. I want to thank Dr. Andrew Thron, for training me on the microscopes and the many associated softwares, and often times providing crucial insight when I needed it most. I want to thank Dr. Xi Cen for his previous work on this project. Though I did not know him personally, I am grateful to him for laying the groundwork upon which my project has been built. In addition, I would like to thank my fellow lab mates Boyi Qu, Joseph Wood, Sean Russell, and JP Stroud for all the times they went out of their way to help and motivate me. I am going to miss the late nights and lively banter that made this journey that much richer.

I am grateful to my parents and sister for their unwavering love and support throughout my entire education, before and at UC Davis. I am here today because they believed in me, often when I did not believe in myself, and provided me with the tools I needed to succeed. Throughout my life, they have served as excellent examples of what can be achieved through hard work and perseverance, and I can only hope to follow in their footsteps. I am thankful to my family in India for their support from the other side of the world, and to the friends I have

made here, who have been my second family while I am far from home and enriched my life immeasurably through their friendship.

I want to express my gratitude to Dr. Roopali Kukreja and her students, for assisting with the deposition of metal layers to create the samples used in this project, and to the CNM2 staff, for training me on the instruments. Lastly, I want to especially thank Dr. Daria Eiteneer, Adam Claydon, Dr. Sabyasachi Sen, and Dr. Subhash Risbud, for reviewing my thesis; they have been instrumental in guiding me in writing my first academic document.

Table of Contents

Abstract

Dewetting is an aspect of materials science that directly affects the reliability of microelectronics and the formation of nanostructures with applications in storage, semiconductors, and plasmonics. Dewetting initiates at triple phase lines between film, substrate, and vapor and propagates away from the triple lines through the process of surface self-diffusion due to film curvature towards flat areas of the film (i.e. away from the edge of a film). As edge retraction starts to occur, other instabilities further the process through allowing agglomeration of the retracting film to form islands of high aspect ratio. The solid-state dewetting and long range edge retraction of Au/Ni thin films from a SiO_2/Si substrate are driven by the minimization of the free surface and film/substrate interface. While dewetting processes in monolayer thin films have been studied extensively, there are only a few studies involving bilayer thin films and only one that reports long-range edge retraction.

This thesis explores the agglomeration and long-range edge retraction of Au/Ni bilayer films from SiO_2/Si substrate. The films were deposited in sequences of Au deposited on top of Ni and Ni deposited on top of Au. As-deposited films were subsequently annealed at 545 ^oC, 675 ^oC, and 730 ^oC. They were characterized by scanning electron microscopy (SEM) and energy dispersive x-ray spectroscopy (EDX) to identify the mechanisms and driving forces for long-range edge retraction. Annealing of Au/Ni bilayer films supported by a SiO_2/Si substrate displayed long-range edge retraction occurring, as well as the formation of seven morphologically distinct regions. The formation of each region was reliant on the dominant mechanisms for retraction at play. Interface and volume diffusion were determined to be the dominant mechanisms in the regions closest to the edge of the substrate (regions P6 and P7), while in the transition region P5,

interface diffusion was the sole dominating mechanism. Surface diffusion dominated regions P3 and P4. The semi-circular shape in which retraction occurred was indicative of a corner instability, the primary mechanism of long-range edge retraction. This is the first reported instance of a corner instability initiating without a corner, especially for long-range edge retraction. Line-like features of high aspect ratio indicated a secondary retraction mechanism of a fingering instability. The comparison between both deposition sequences revealed the stabilizing effect a native NiO_x has on the bilayer film through hindering edge retraction and the critical role that interaction between Au and Ni plays in edge retraction. A uniform area of dark contrast indicating the Si substrate at the P2-P3 interface was observed in all Au/Ni bilayer films. It was proposed that this interface is a result of void formation and nucleation propagated by a thickness variation in region P2 due to the diffusion of Ni to region P3. However, another explanation is the occurrence of a pinch-off event due to the agglomeration of Au and Ni in regions P3 to P5 reaching a critical height. However, additional data is required to ascertain whether that is occurring.

1. Introduction

Wetting is associated as a phenomenon of equilibrium thermodynamics due to being a measure of the interfacial energy between two bulk phases and used to determine the rate of spreading of a liquid in a contact area with a solid [1]. Spreading is the concept that if a drop of liquid were placed on a solid surface, it will spread to cover the solid surface until it reaches a state of equilibrium. The extent to which the drop of liquid spreads is dependent on the properties of the materials used and the environmental conditions [29]. Dewetting is defined as the kinetic process through which a bulk phase agglomerates into droplets, following the spreading process in reverse. It is a result of underlying imbalances between the interface and surface free energies of the deposited thin films [30]. Any processes that involve adhesion or splitting of two or more separate materials can be referred to as wetting and dewetting. These transitions are often observed during microstructure formation, including sintering and grain growth. Some applications for wetting-dewetting mechanisms include catalyst-activated growth of nanostructures, such as semiconductor nanowires or carbon nanotubes [15-22], catalysts for hydrogen storage [14], the formation of Schottky barriers [12] and nanoparticles for plasmonics [13].

As wetting-dewetting are well-established processes in materials science, the mechanisms that initiate and propagate these processes have been studied extensively in monolayer films of various materials and substrates. A mechanism for the agglomeration of polycrystalline films is grain boundary grooving. A groove is where the grain boundaries intersect the surface of the polycrystalline film [31-33] and is caused by surface atoms moving away from the grain

boundary due to surface diffusion. Grooves forming at the surface is an intermediary step to the formation of holes. An alternate mechanism for the formation of holes is the formation and growth of voids, which are a result of instabilities at the triple junction between the grain boundaries in the film and the film/surface interface [34-36].

For bilayer or alloyed thin films, the interaction of the different components and external conditions will determine how agglomeration occurs. Few studies have explored the mechanisms that affect wetting-dewetting transitions in bilayer films. One explored the effects of alloying Au with small amounts of Pt, resulting in a slight resistance to the onset of dewetting at low temperatures, as compared to a single film of Au [23]. A study involving dewetting of Ni-Ag alloyed films showed that the addition of immiscible Ag in Ni results in fractal-like growth of holes instead of the expected capillarity driven nucleation and growth of holes initiated by grain boundary grooving [24]. For alloyed Ni-Cr films [25] different annealing conditions resulted in various dewetting kinetics due to surface oxidation and film-substrate interaction. A study utilizing nanosecond pulsed laser melting to induce dewetting of an Ag and Co [26] bilayer films showed spinodal instabilities forming in the film, which were caused by concentration gradients introduced by film deposition sequence and solubility. Au/Fe and Fe/Pd bilayer films [27,28] showed enhanced thermal stability upon annealing due to the alloying effects. Au/Ni bilayer films on prepatterned and flat SiO_2/Si substrates revealed new features forming due to alloying that could allow for designing of novel array nanostructures [39].

For this Master of Science project, bilayer films of Au and Ni were selected as this is a continuation of previous studies conducted by Xi Cen and coworkers [10]. Au and Ni are not ideal materials to study dewetting, but they were initially selected due to the miscibility gap

and limited alloying effects of the two elements up to a temperature of 675 °C. Previous studies had noted that dewetting occurs locally due to both grain boundary grooving at the surface of the film and void formation at the interface between the bottom metal film and the substrate. It was assumed that this occurs throughout the entire length of the substrate/bilayer film interface. Schaaf et al conducted multiple studies on Au/Ni bilayer films and reported a strong correlation between number of voids per unit area and variations in thickness ratio [61, 62] and a metastable phase formation above the bulk equilibrium solubility which makes the breakup of the Au/Ni bilayer film less likely. However, the work by Schaaf et al did not exhibit long-range edge retraction. There is only one previous study that has reported long range edge retraction in a single layer Ni film, which had retracted less than a distance of 5 μm [11]. A recent study conducted by Cen et al. reported long range edge retraction in Au/Ni bilayer films that spanned distances of more than 200 μm as well as distinctive regions created by the retraction of the bilayer film [10]. While the study had been the first to note distinctive regions that occur with long-range edge retraction insufficient data was presented to determine the mechanisms that drive long-range edge retraction. Multiple studies by Zucker et al have introduced mechanisms for edge retraction and dewetting including fingering instabilities, corner instabilities, and hole formation [3, 7, 33] . As a continuation of the study by Cen et al, this project has examined the effects of different deposition sequences and annealing temperatures on metal bilayer film agglomeration, and attempts to identify potential mechanisms for long-range edge retraction and the formation of different distinct regions previously observed.

2. Literature Review

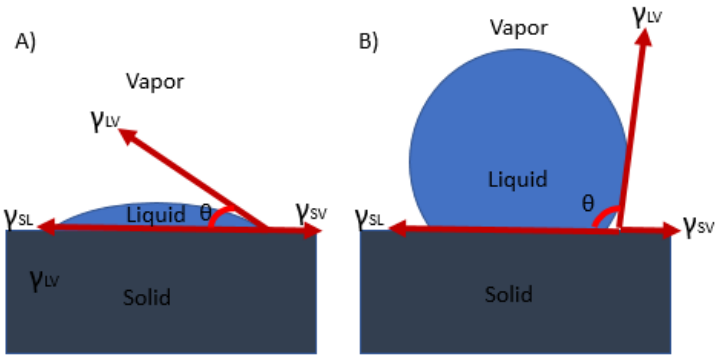

Figure 1: *Examples of partial wetting behavior; (a) good wetting, (b) bad wetting.*

Figure 1 shows three distinct bulk phases, a solid phase, a liquid phase, and a gas phase. The solid phase represents the substrate, the liquid phase represents a deposited material supported by the substrate surface, and the gas phase (vapor) surrounding the film and covering the free substrate surface. Interfaces between the solid and liquid phases, the liquid and gas phases, and the solid and gas phases each have interfacial energies associated with them. If at least one of the two phases in contact at an interface is crystalline, the energy of the interface may be anisotropic [7]. The contact angle θ_Y is denoted in the diagram. This angle can be calculated using the Young's equation [1]:

$$\cos \theta_Y = \frac{\gamma SV - \gamma SL}{\gamma LV} \qquad \text{(equation 1)}$$

In the above equation, γ_{SV} is the interfacial energy between the solid and the gas phase, γ_{SL} is the interfacial energy between the solid and the liquid phase, γ_{LV} is the interfacial energy between the liquid and the gas phase, and θ_Y is the Young contact angle. The equation is based on a

method of comparison between the interfacial energies of the bulk phases in the diagram and leads to define the accepted contact angle parameters for conditions for complete wetting, partial wetting, and non-wetting [1]. Complete wetting is defined as a contact angle that is 0^o. Non-wetting is defined by a contact angle of greater than 90^o. Partial wetting is defined as a contact angle of anything between 0^o and 180^o. Often, a contact angle greater than 90^o is referred to as "bad wetting", while a contact angle of less than 90^o is referred to as "good wetting" [1]. Although Young's equation is fundamental to the definition of wetting, it makes the following assumptions: no chemical interactions occur between the liquid phase and the substrate; surface energies are isotropic, and the film is liquid. As none of these assumptions are true for a solid-state bilayer thin film, a more appropriate equation describing the balance of surface and interface energies between crystalline solids is Herring's equation:

$$\sum_{i=1}^{3} \left(\gamma_i \vec{t}_i + \frac{\partial \gamma_i}{\partial \vec{t}_i} \right) = 0 \qquad \text{(Equation 2)}$$

Herring's equation describes thermodynamic equilibrium at a triple line of a thin film. $\gamma_i$represent the three interfacial energies at the triple line. $\vec{t}_i$is a vector normal to the triple line, in the plane of the ith interface. The $\frac{\partial \gamma_i}{\partial \vec{t}_i}$ term represents the torque and is perpendicular to $\vec{t}_i$ and the triple line [1].

While the discussion thus far has focused on the thermodynamics of wetting, discussion from this point forward will concentrate on the kinetic process of dewetting. Some of the key kinetic features of dewetting include edge retraction, hole formation, thickening of the rim, and the

break-up of the film into island-like structures or fingers. Most of these occur at the edges of the thin film due to the prevalence of defects.

2.1 Edge Retraction

One of the key features of dewetting is edge retraction, which happens when a rim of a previously uniform thin film recedes from the edge of the substrate after being annealed at high temperatures.

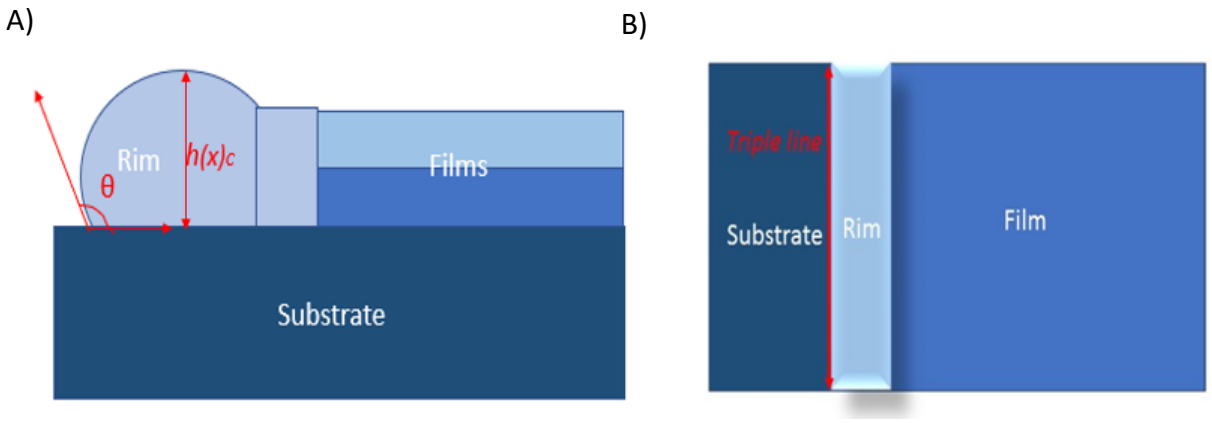

Figure 2: *Edge retraction from a) cross-sectional view normal to the triple line and b) top view.*

Edge retraction rates can reveal important information about the mechanisms of mass flux. The initial comparison of such was conducted by Brandon and Bradshaw [39] who utilized the assumptions that the rim of the film is a semi-circle, and the contact angle is 90^{o}. However, the model was developed to determine how a hole is formed, rather than to observe edge retraction from a straight edge, or a uniform edge of a substrate as shown in Figure 2 [38].

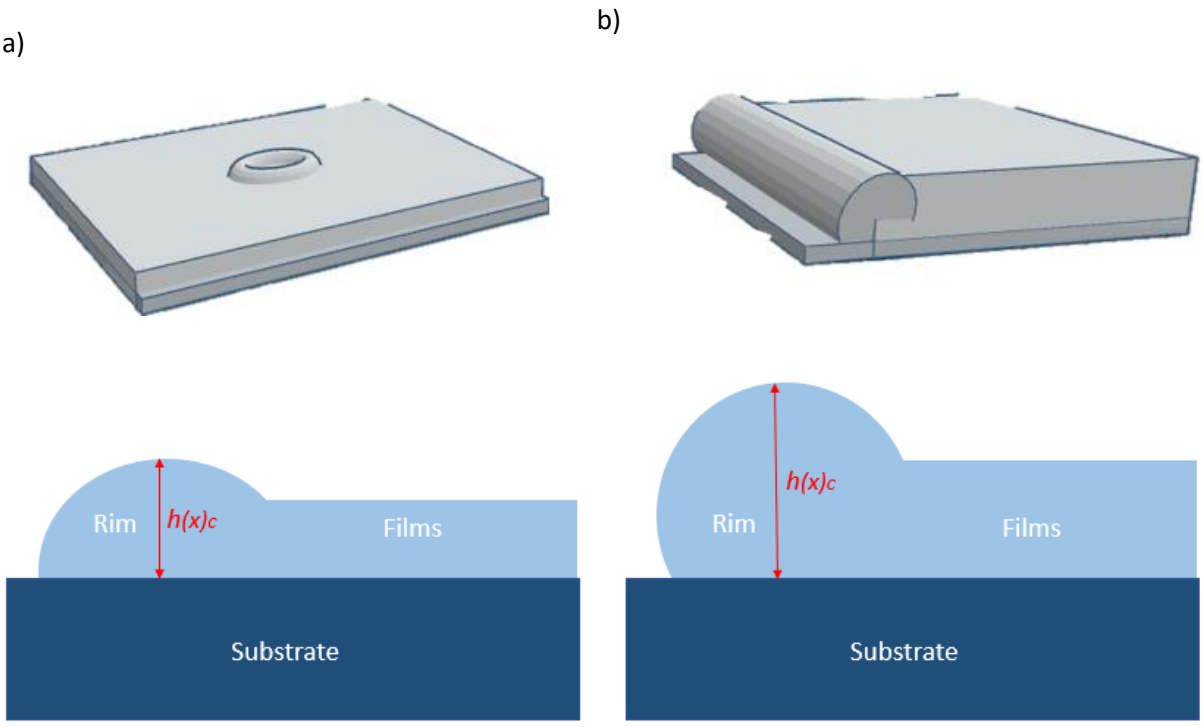

Figure 3: *A visual representation of a) a hole (top) and the corresponding semicircular cross-sectional profile of the rim (bottom) as dictated by Brandon and Bradshaw [38] and b) a model of a straight edge (top) and the corresponding cross-sectional profile of a rim intersected by chords as dictated by Zucker et al [7].*

The comparison of the retraction rate is determined by the theoretical change in the volume of the rim with time as retraction occurs based on the model for each case, the hole and the straight edge. The key differences in the models are that while the rim is assumed to be a semi-circle in the hole model, in the straight edge model, the rim is assumed to be a circle intersected with a chord. This creates a difference in the volume that can be attributed to the rim in each case. Another key difference is that the straight edge model assumes a contact angle that can be varied so the retraction rate can be determined as a function of any chosen contact angle [7].

The different dimensions of the rims in both cases also creates a difference in the rate at which the volume changes. Based on this comparison, it was determined that rate of the change in volume is 2.8 times higher for a hole than it is for a straight edge [7].

A more accurate geometric model which assumes that the initial geometry of a rim is representative of a quarter of a circle and the contact angle is variable, can also be theoretically tested for the retraction velocity [7]. The graph in Figure 4 was generated using the assumption of the shape of the rim from Figure 3b and the following equations relating the retraction velocity (v_{retr}) with the rim height, and the rim height with retraction time leading to the retraction distance as a function of time [7].

$$r = \frac{h}{1 - cos\theta} \qquad \text{(Equation 3.1)}$$

The above equation relates the rim height (h) to the radius of curvature (r) and the contact angle (θ). The relation was used to calculate a retraction velocity as a function of the rim height (Eq. 3.2) [7].

$$\nu_{retr} \approx \frac{csc\theta(cos\theta - 1)^3}{h^3\,(\theta + arcsin(\frac{1}{h}\,sin(\frac{\theta}{2})\sqrt{2(h-1)(1+h+(h-1)cos\theta)}\,))^2} \qquad \text{(Equation 3.2)}$$

$$h(t_2) = h(t_1) + \alpha v_{retr}\, dt_1 \qquad \text{(Equation 3.3)}$$

$$h'(t) = \alpha v_{retr} \qquad \text{(Equation 3.4)}$$

The rim height was then determined as a function of time (Eq. 3.3) below where α (rim height as a function of time) is the quantity being solved for and dt_1 can be assumed to be 1 due to the negligible dependence of α on it. As such, the final equation relating the retraction distance as a function of time (Eq. 3.4) is derived [7].

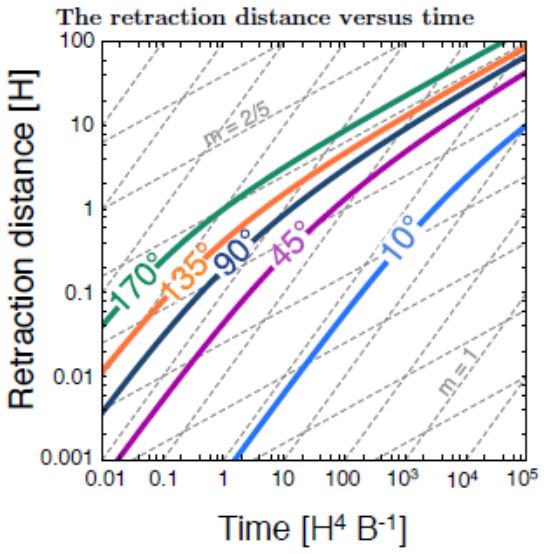

Figure 4: *Relationship between the normalized retraction distance and time as a function of contact angle in which H is film thickness and B is the material constant, showing the rate of retraction as dependent on the contact angle [7]. Reprinted with kind permission from MIT, Ref. 7.*

The trend shows the larger angles retracting the largest distance in the same amount of time, meaning the retraction velocity is greater. Furthermore, the trend of retraction or the retraction rate, the slope, changes from ½ to 2/5 in small time scales for the larger angles, while the time scales increase to make that transition as the angle decreases. Since many metals have a contact angle of 90^o [1], it can be assumed that the transition from a linear slope to a slope of 2/5 is too quick for the linear slope to even be detected. [7] As such, the contact angle of the retracting edge can be an indication of the retraction rate of the edge.

2.2 Pinch-off Events

Most often, a film is observed retracting from the edge and moving inwards. Retraction often causes the rim of the film to thicken and a valley to form ahead of the retracting rim [8]. The height of the valley varies but it is often an order of magnitude smaller in height than the rim [7]. The rim growing causes the valley to also deepen. At a certain point during film retraction, the valley depletes and approaches the underlying substrate. This is called a pinch-off event. Pinch-off events occur in a cyclic pattern as retraction occurs [9].

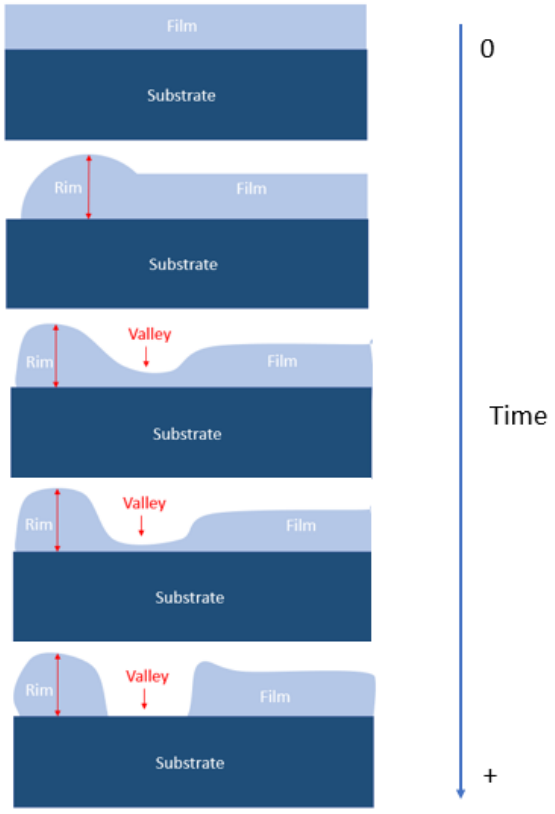

Figure 5: *Schematic of the progression of a pinch-off event occurring over a period of time.*

2.3 Fingering instabilities

The fingering instability is an instability caused by different thicknesses of the rim due to uneven mass transport along the rim, resulting in finger-like structures forming as edge retraction occurs.

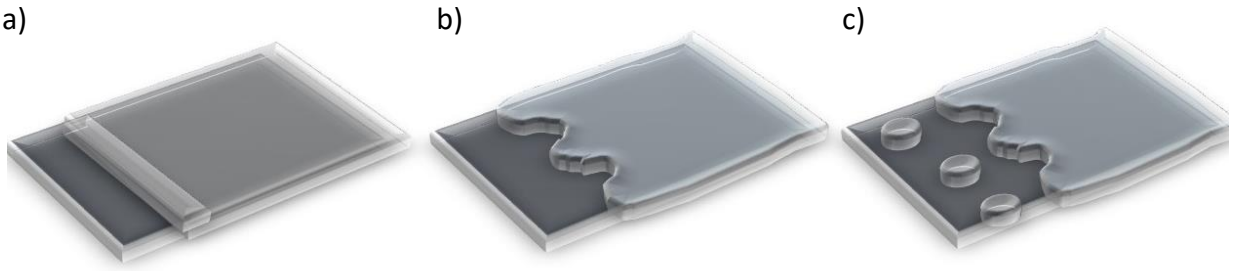

Figure 6: *Progression of fingering instability in which a) is representative of the film starting to retract with a visible rim, which leads to the formation of fingers, as shown in b) and progresses to the formation the tips of the fingers breaking up and forming islands, as seen in c).*

It is observed for single crystal and polycrystalline films alike. The two distinguishing characteristics of the fingering instability are the differences in the triple line position or curvature, and the differences in the rim height. There are three possible causes for the fingering instability. They are recognized as instabilities of their own which each contribute to the fingering instability and include: (1) the Rayleigh-like instability, (2) the divergent instability, and (3) the arc length instability [7.

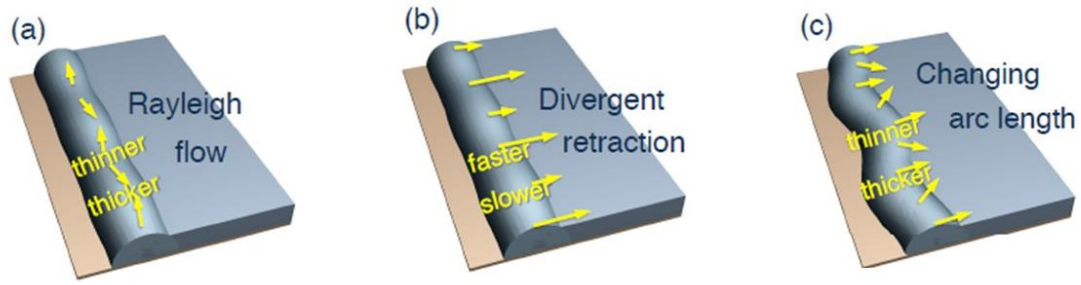

Figure 7: *The Rayleigh-like, divergent, and arc length instabilities are displayed above in a progression of occurrence. a) the Rayleigh-like instability shows the thickening and thinning of different parts of the rim, b) the divergent instability shows the different rates at which the rim retracts in relation to the thickness, and c) is the arc length instability, which shows the changing arc length of different sections of the rim and a start to the formation of fingers. Reprinted with kind permission from MIT, Ref 7.*

2.3.1 Rayleigh-like instability

The Rayleigh-like instability is fundamentally the instability of a cylinder-like structure, which is representative of the rim. It causes the structure to separate into individual spheres to minimize the surface energy. The cause of the instability is the perturbations instigated from defects or anisotropy that the cylinder-like structure is subject to which lead to mass transfer in the rim. As a result, mass in the rim is unevenly distributed, so that there are sections of the rim that are thicker as compared to others [7]. Perturbations are sometimes introduced deliberately through a process called stepping to induce a fingering instability [37].

a)

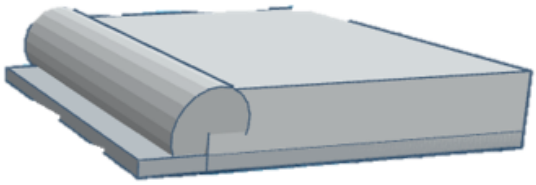

b

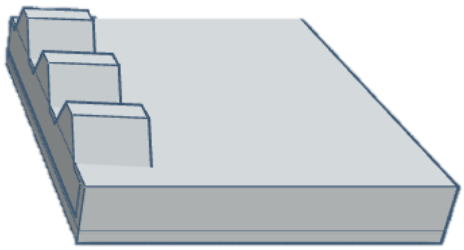

Figure 8: *a) An unperturbed film and b) a perturbed film due to small surface defects or anisotropy.*

The rim in Figure 8b shows a periodic variation in rim thickness, which is described a wavelength. The wavelength has to be at least half the circumference of the cylinder for the instability to develop due to the difference in thickness of the rim. Mass transport is the driving force which allows this to occur and is instigated by the application of heat. It was determined in previous studies that the perturbation wavelength that results in the fastest rate of surface diffusion, or the fastest growth of the perturbation, is 8.88r, where r = $\frac{h(x)}{2}$ [6]. As such, the following equations govern the perturbation growth rate of the Rayleigh-like instability in which κ is the mean curvature of the rim and s_1 and s_2 denote different directions [7]:

$$\frac{\partial^2 \kappa}{\partial s_2^2} \approx \frac{\kappa(s_1, 2\Delta s_2) - 2\kappa(s_1, \Delta s_2) + \kappa(s_1, 0)}{(\Delta s_2)^2}$$

(Equation 4.1)

$$\mathrm{GR}_{\text{Rayleigh-like}} = \frac{1}{\sin\theta}\left(\frac{\partial^2 \kappa}{\partial s_1^2}\Big|_{x=0, s_2=0} - \frac{\partial^2 \kappa}{\partial s_1^2}\Big|_{x=\pi/k, s_2=0}\right)$$

(Equation 4.1)

2.3.2 Divergent Retraction Instability

The divergent retraction instability is the difference in the retraction rates of the rim based on different thicknesses in parts of the rim. Areas of different thickness form due to the transfer of mass perpendicular to the triple line. The thicker areas of the rim are slower to retract than the thinner areas. This creates a difference in the retraction distances covered by areas of the rim. The average curvature of the rim is defined to be 1/h(x), where h(x) is the rim height. This is in comparison to the curvature of the flat film, which is zero. The distance from the triple line to the film is $\frac{\pi}{2*h(x)}$, due to the model cross-section being that of a quarter of a circle. From this equation, the gradient of the curvature can be determined by integrating the distance, with a result of $\frac{1}{h(x)\text{^}2}$ [7]. The gradient of curvature is a factor in determining the occurrence of a pinch-off event. The gradient of curvature normal to the triple line is a driving force for edge retraction. Mass transfer normal to the triple line is the driving force for the divergent retraction instability. As such, differences in the rim height, h(x), and therefore, in the gradient of curvature, also cause differences in the retraction rate. As such, the following equation govern the perturbation growth rate of the divergent instability [7]:

$$\mathrm{GR}_{\text{Divergent retraction}} = \frac{1}{\sin\theta}\left(\frac{\partial^2\kappa}{\partial s_2^2}\Big|_{x=0,s_2=0} - \frac{\partial^2\kappa}{\partial s_2^2}\Big|_{x=\pi/k,s_2=0}\right) \quad \text{(Equation 5)}$$

2.3.3 Arc Length Instability

The arc length instability is a variation in arc length in which the mass transfer that occurs with the progression of the instability is normal to the triple line. Additionally, a perturbation in the triple line adds more curvature to the gradient as it propagates into the film, as shown in Figure 5c, before decaying.

a) b)

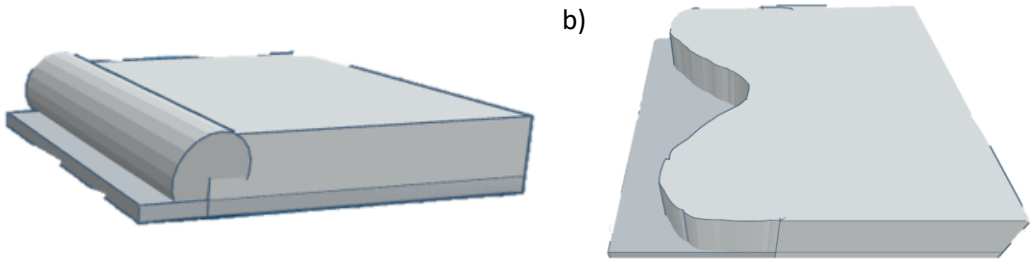

Figure 9: *a) An unperturbed film and b) a perturbed film as pertaining to an arc length instability due to the triple line moving into the film.*

When retraction occurs, the edge moves towards the film. If the triple line moves into the film, it creates a negative curvature into the film as shown in Figure 9b. The negative curvature distributes the mass of the rim across a wider distance, normal to the triple line. As a result, the height of the rim, as compared to a straight edge, also decreases to compensate for the spreading mass. As this creates a thinner rim, the retraction velocity increases due to less mass per the area [7]. As such, the following equations govern the perturbation growth rate of the arc length instability [7]:

$$\mathrm{GR}_{\text{changing arc length}} = \Big(\alpha(x)\, v_{\mathrm{retr}}(x)\Big)\Big|_{h(x)=1+\eta,\, \kappa(x)=+\epsilon k^2} - \Big(\alpha(x)\, v_{\mathrm{retr}}(x)\Big)\Big|_{h(x)=1+\eta,\, \kappa(x)=-\epsilon k^2}$$

(Equation 6)

2.3.4 Combined Effects

The Rayleigh-like instability is one of the three mechanisms that could explain the cause of fingering instabilities. It is wavelength-dependent and plays a critical role in determining the critical wavelength for fingering instability [37]. If we assume a contact angle of 90^o in this case, the behavior of the Rayleigh-like instability can be likened to a cylindrical case, due to it being a metastable shape, giving a critical wavelength of $2\pi r$ and a fastest growing wavelength of $2.83\pi r$, where r is the radius of curvature of the rim. The Rayleigh-like instability exists when there are large perturbations at play, providing a fastest-growing wavelength. However, a decrease in the contact angle and in the perturbation amplitude causes the effect of Rayleigh-like instability to decrease as well. The divergent retraction instability, however, still stays in effect. The divergent retraction instability grows the fastest at long wavelengths. As the perturbation advances the triple line in areas with a lower rim thickness, introduces curvature to the triple line, which introduces wavelength dependence, as it affects the driving force. Since this affects the driving force, it also introduces wavelength dependence. The divergent retraction instability is dominant for critical wavelength behavior for small perturbations. When the critical wavelength is zero, the same behavior is seen in the fingering instability. The fastest growing perturbation is observed for long wavelength for divergent retraction and for fingering instability when the contact angle is less than 57.4^o [7]. The divergent instability is responsible for shifting to longer wavelengths. In contrast, the arc length instability is only significant for very short wavelengths. If the wavelength of perturbation is shorter than a certain limit, it will cause the thin sections of the rim to get thinner while the edge is retracting. This is caused by the triple line expanding without enough volume from the film being swept up to keep the rim

height constant. The arc length instability is important when the interface energies between the substrate and film are anisotropic [7].

The perturbation growth is constant for any wavelength longer than the fastest wavelength, but even in that case, the distance between two peaks will be between the value of the fastest wavelength and the twice the value of the fastest wavelength. Some of the points to note about all the instabilities are that an increasing rim height is the cause of a slowing growth rate. The formation of fingers is due to the slowing growth rate in some areas. Since the disparity in growth rates only increases, no new fingers can form after finger formation has started. However, fingers may merge together, leading to larger spacing between them. A higher contact angle is also more likely to lead to fingering due to the decrease in the critical wavelength, allowing the shorter wavelength perturbations to grow. As the perturbation size increases, the critical wavelength also increases but the perturbation growth decreases due to the domination of the Rayleigh-like instability. When the perturbation size is small, the Rayleigh-like and arc length instabilities do not affect the critical and fastest wavelength values, only the divergent instability does. Due to this factor, the divergent instability can be considered the main cause of the fingering instability [7].

2.4 Corner Instability

Corner instability occurs on anisotropic films and starts at a point where two edges intersect. The figure below is a representation of a corner instability.

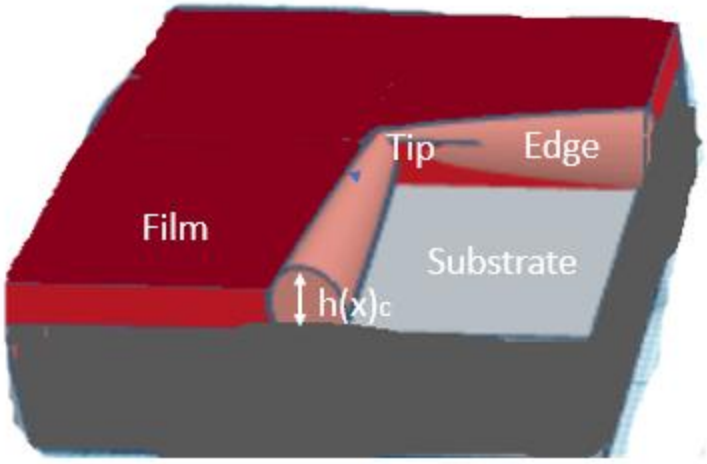

Figure 10: *A corner instability with various sections labeled such as the edge, tip, film, substrate, and height of the edge and tip in comparison to that of the rest of the film*

At first, the corner and the edge retract at the same rate, but over time, the retraction rate of the edge slows down while the retraction rate of the corner stays constant. This observation is a direct consequence of the difference in what occurs with the rim heights of the corner as opposed to the edge. The rim height at the corner stays constant throughout retraction while the rim height at the edge increases with retraction. The increase in the rim height slows down retraction at the edge, while the maintenance of the rim height allows for the continuation of retraction at the corner [2]. One explanation of this occurrence was that the mass that is swept up during retraction flows away from the tip of the corner and onto the flat film [3]. This is possible due to the two-dimensional diffusion at the tip of the corner, allowing mass to be transported to a larger area and speeding up retraction at the tip [4]. Another proposed explanation was that the mass swept up during retraction flows from the corner to the center of the edge rim [5].

Zucker proposed a model in which different regions are established: the tip, where the instability originates and progresses, the transition region, and the edge, which is assumed to be a straight edge of uniform rim height. There is a linear increase in rim height from the tip to the edge, and a constant angle between the tip and the transition region. As retraction at the tip progresses, the film that is swept up adds volume to the rim, which, in turn, increases the rim height. However, for the retraction to progress, the arc of the tip also has to lengthen due to the in-plane curvature of the triple line, causing a decrease in the rim height. At the beginning of retraction, the volume addition to the rim is favored, and the continuing retraction allows for the rim to become thinner until it reaches a state of equilibrium, with the volume added to the rim being the same as the volume used to lengthen the rim. This process indicates that there is no long-range mass transport occurring. A similar process occurs during the growth of a hole, with the difference that mass is added to the rim, causing the rim to grow in height. However, due to the limited elongation of the rim, the thinning effect does not occur, causing the growth of the hole to be slowed and eventually stopped over time. [7]

3. Methods

3.1 Deposition of metal thin films

Au and Ni bilayer films were deposited on a Si substrate in consecutive steps, each layer was deposited with a nominal thickness of 30 nm. Prior to metal deposition, the Si substrate was covered with a thermally grown SiO_2 film with a thickness of 12 nm to prevent the formation of silicides and metal diffusion into the substrate. The metal layers were deposited in two sequences as illustrated in the figure 6:

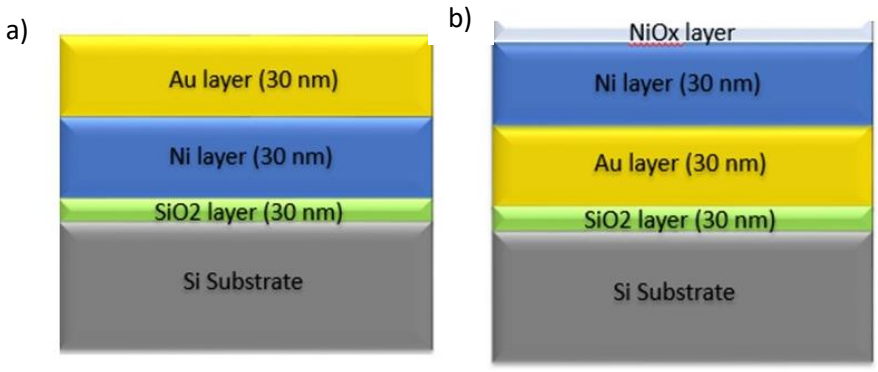

Figure 11: *Sketch of the deposition sequences; a) is Au deposited on top of Ni while b) is Ni deposited on top of Au.*

Metal layer deposition was carried out with an AJA Orion 8 Ultra-High Vacuum DC sputtering system under Ar gas atmosphere. The vacuum was not broken between the deposition of each metal layer, ensuring that the Ni layer did not oxidize and form a native NiO_x layer between the two metal layers. The Ni layer was deposited at 162 W power, at a rate of 0.67 Å/s, a chamber pressure of 3.1 E-6 torr, and an Ar flow rate of 30 sccm. The Au layer was deposited at 49 W power, resulting in a rate of 1.07 Å/s. The chamber pressure and the Ar flow rate were the

same as those utilized for the Ni layer deposition. Prior to deposition, the substrates were cleaned with methanol and dried under flow of dry N_2 gas.

3.2 Annealing of as-deposited films

As-deposited metal bilayer films were rapid thermally annealed in a vacuum tube furnace. Samples of each deposition sequence were placed in an alumina boat and inserted into the glass tube well outside the hot zone of the furnace. The tube was then evacuated to a base pressure of roughly 1.1E-4 Pa. The tube furnace was set to a temperature of 545 ^{o}C and stabilized at that temperature over the course of 4 hours. When thermal stability was reached, the samples were inserted into the hot zone of the furnace by sliding the vacuum tube over the span of one minute, which corresponds to a heating rate of roughly 545 ^{o}C/min. Samples were annealed in the center of the furnace for one hour. Thereafter, the tube was pulled out from the furnace to place the sample in an area with a temperature below 100 ^{o}C. In this configuration mass transport is considered insignificant compared to the annealing process. The samples were allowed to cool to room temperature under vacuum for a period of several hours before being taken out of the tube furnace. This procedure was repeated for different samples with annealing temperatures of 675 ^{o}C and 730 ^{o}C.

3.3 Characterization

3.3.1 Imaging

The film morphologies after rapid thermal annealing were characterized with a Thermo Fisher Scientific Quattro Environmental Scanning Electron Microscope (ESEM). Electron micrographs were recorded with an Everhart-Thornley detector, with a positive collector bias. This detector configuration collected a mix of secondary and back-scattered electrons. For the purposes of this study, bright intensities will be considered higher atomic number of the scattering element. The MAPS 2.0 software package was utilized to image a large section of each sample by automatically collecting high magnification SEM images and subsequently merging them together to form a micrograph with high magnification and large field of view. Individual micrographs were merged by maximizing the cross-correlation function in regions of mutual overlap.

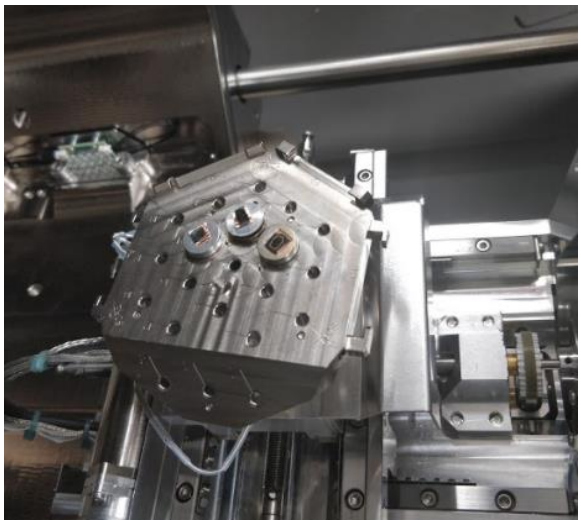

Figure 12: *The image above is of Au/Ni bilayer film samples being loaded into the SEM chamber for characterization.*

3.3.2 Spectroscopy

Energy dispersive x-ray spectroscopy measurements were carried out at room temperature and under high vacuum conditions to determine projection views of elemental distributions. EDXS data were collected with a Bruker Quantax 400 XFlash 6 solid state detector attached to the ESEM. EDXS data were collected from areas of the sample that displayed characteristic regions of edge retraction. Integrated EDX intensity versus distance graphs were collected via a modified line graph that vertically averaged EDX intensity from selected regions of interest. Specific intensities were obtained through background subtraction and standardless quantification, without correcting for absorption.

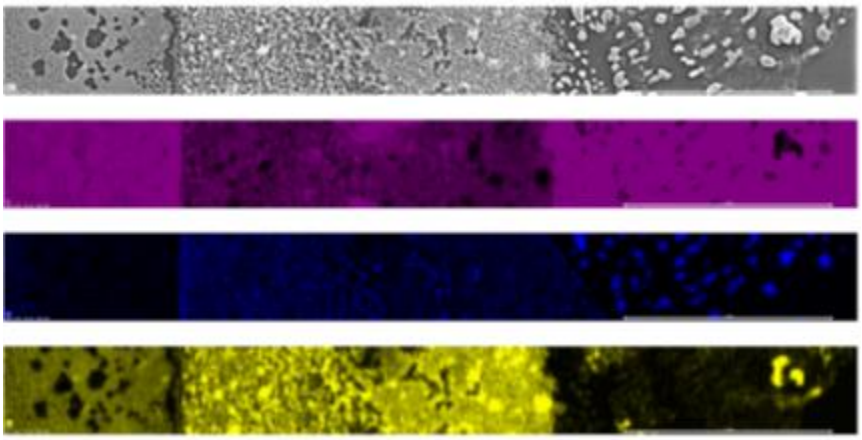

Figure 13: *The figure above is an EDX image showing an example of the chemical distribution of the SEM image above, along with Si (purple), Ni (blue), and Au (yellow).*

3.3.3 Image Analysis

The calculation of curvature ratios of the triple line was carried out with the use of the ImageJ software package. The point mapping feature was employed to accurately trace the curve of

each distinct interface. Each interface was traced with a set number of 100 evenly spaced points and straightening the curve using a “straightening tool”. This process was iterated five times for each curve of all the six samples to provide the most accurate measurement of the curvature of each interface by counting the number of image pixels along the traced line (see Figure 14). The same curve was measured from end to end with a straight line to determine the curvature trio of each interface.

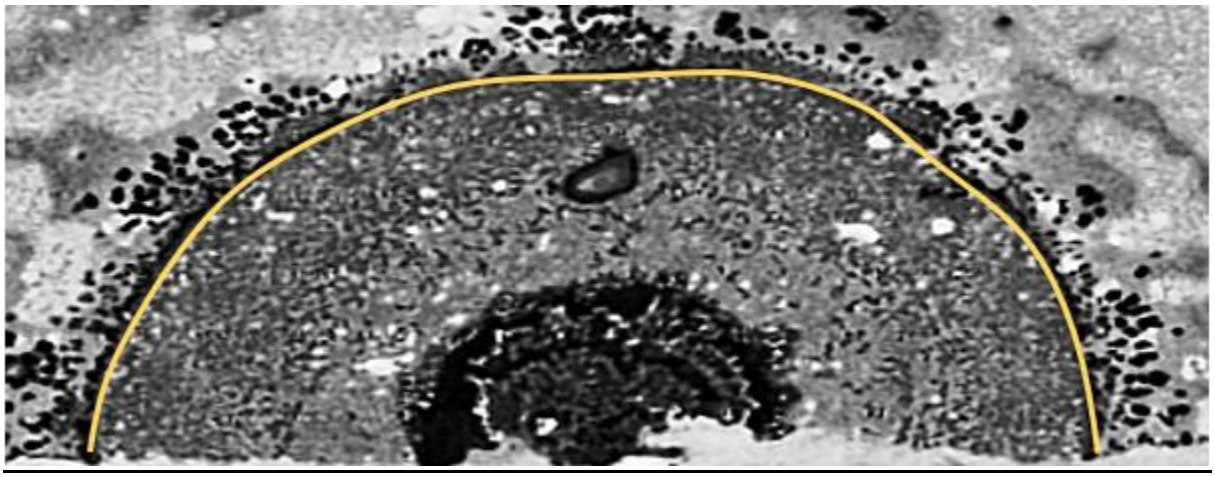

Figure 14: *The figure above is a MAPS micrograph showing an example area from which curvature data was extracted.*

4. Results

4.1 Imaging

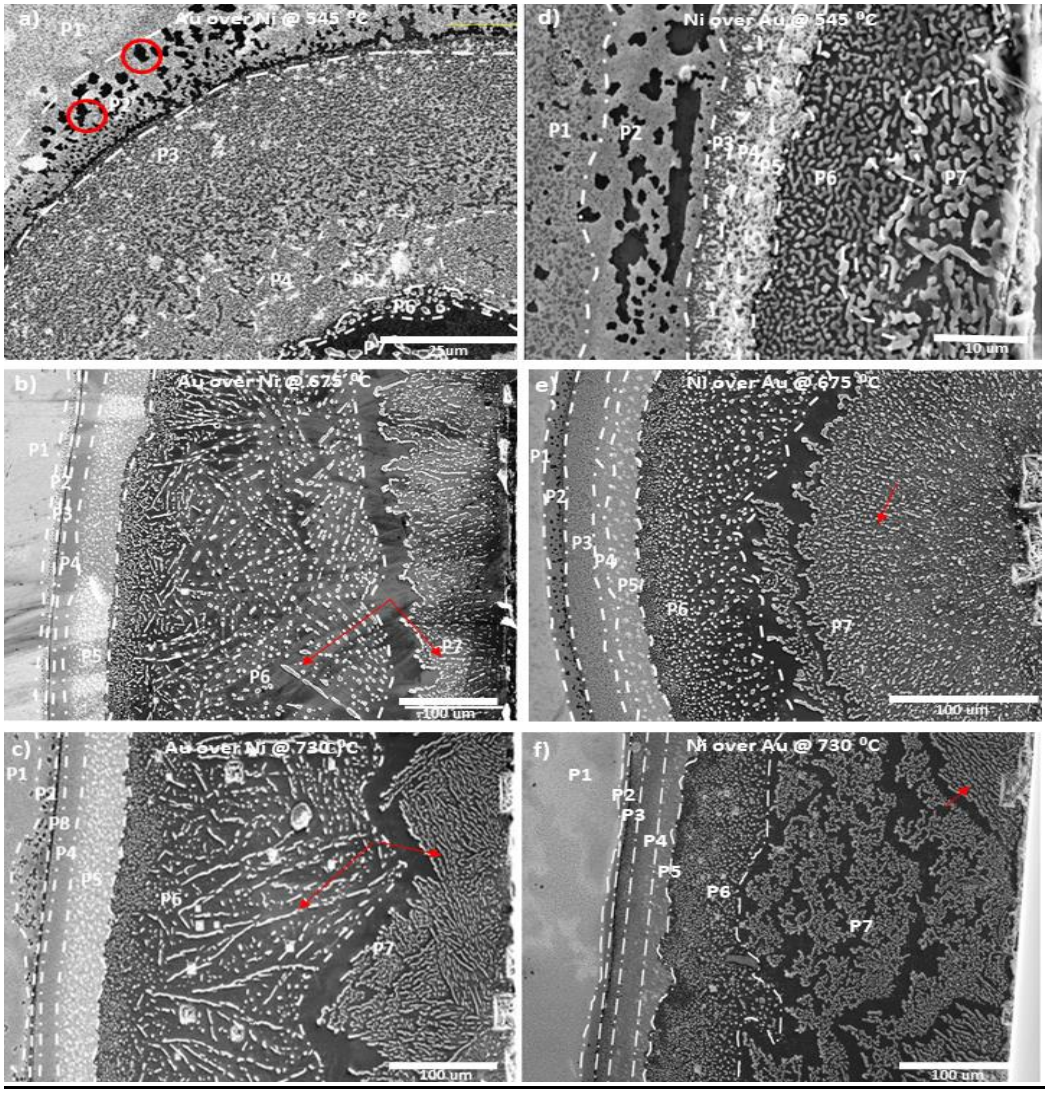

Figure 15: *Micrographs of all samples via SEM with distinctive regions separated by a dashed line and labeled P1 to P7 (center to edge); a) is Au deposited on top of Ni and annealed at 545 °C b) is Au deposited on top of Ni and annealed at 675 °C , c) is Au deposited on top of Ni and annealed at 730 °C , d) is Ni deposited on top of Au and annealed at 545 °C , e) is Ni deposited on top of Au and annealed at 675 °C , f) is Ni deposited on top of Au and annealed at 730 °C .*

Figure 15 shows SEM micrographs of the annealed metal bilayer films. The left column is comprised of samples of sequence A (Au deposited over Ni) while the right column shows images of sequence B (Ni deposited over Au). Bilayer films in A) and B) were annealed at 545 ^{o}C, those in C) and D) were annealed at 675 ^{o}C, and those in E) and F) were annealed at 730 ^{o}C. After annealing all bilayer films revealed seven regions with distinctly different morphologies. Dashed lines indicate borders between regions marked P1 through P7. The different regions are distinguished by their unique morphologies and microstructures. The edge of each of the sample is on the right side of the image, with the region P7 as closest to the edge and P1 extending towards the center of the substrate wafer. While the morphology of each region is similar across all samples, the average width of each region depends on the annealing temperature and deposition sequence (see Table 1).

The region marked P1 in Figure 15a shows a patchy morphology with dark and bright areas, representative of Ni and Au, respectively. The dark grey/black areas are indicative of the Si substrate. Region P1 shows a mix of Au and Ni. Region P2 has a similar morphology as P1 but appears darker in comparison. Holes with a fractal morphology are present across the entire P2 region, referenced by the red circles in Figure 15a. The largest holes are along the interface between regions P1 and P2 and the smallest are close to the interface with P3. The interface between regions P2 and P3 is a line-like gap with the Si substrate visible as black contrast. In region P3, Au and Ni have agglomerated locally, with some small bright spots which represent Au-dominant areas, and larger dark spots which are Ni-dominant areas, with the Si substrate visible in some areas. In contrast to P3, regions P4 and P5 are more uniform in their morphologies. However, region P5 reveals large agglomerations of Au. These are concentrated

close to the interface between P5 and P6. In the P6 region, there is no continuous film detected and relatively small islands of Ni can be observed. Region P7 shows large islands of agglomerated Ni. With the lack of a continuous film, most of the P6 and P7 regions show black contrast, i.e. the Si substrate, underneath.

Figure 15b shows Au deposited onto Ni and annealed at 675 ^{o}C. The distinct regions in the micrograph extend over 400 μm in total as compared to those in Figure 15a. In region P1, the film displays a bright contrast, indicating presence of Au, with spots of darker contrast, indicative of the Ni layer underneath the Au layer. Region P2 appears darker than P1 overall, indicating presence of more Ni or a larger Ni to Au ratio. There are small holes present throughout the region. The interface between the P2 and P3 regions is characterized by a continuous thin gap of black contrast observed across the sample, indicating the absence of Ni and Au. The P3 region, exhibits an agglomeration of Au along the interface of the region, close to the gap between regions P2 and P3, with the rest of the region presenting localized agglomeration of Au and Ni. The P4 region is a more even mix of Au and Ni. The P5 region is distinguishable due to large agglomeration of Au and a more homogeneous darker contrast representing underlying layer of Ni. The interface of the P6 region shows smaller agglomerated islands of Ni with black contrast of the substrate underneath. The size of the agglomerated Ni islands increases with proximity to the P6-P7 interface, with the largest and most widely dispersed islands observed along the P6-P7 interface. Long formations of agglomerated Ni stretching from the edge of the substrate wafer towards the center with a “line-like” appearance can be observed in regions P6 and P7, marked by red arrows in Figures 11b, c, e, and f. The line-like formations observed in P7 are more continuous in comparison to those in

region P6 but are also smaller in size. A significant gap is observed between the P6 and P7 regions, with intensities representing the substrate. The interface of the P7 region is lined with large agglomerations of Ni continuous along the border.

In region P1 of Figure 15c, an even mix of both Au and Ni is present. A majority of the area shows bright contrast representing Au, with some smaller hole-like formations that show darker intensity representing Ni. In P2, even though a morphology similar to P1 is observed, there are larger number of holes present in the film and the region appears overall darker compared to P1. The gap between regions P2 and P3 is characterized by a continuous dark line. In the P3 region, there is an agglomeration of Au along the P2-P3 interface with the rest of the region being an even mix of Au and Ni. The P4 region shows small agglomerations of Au with an otherwise uniform layer of Ni. The P5 region is similar to P4 but the agglomerated Au islands are much larger in size. The area of the P6 region closest to the P5-P6 interface shows smaller agglomeration of Ni with the substrate visible. The line-like formations that were observed in Figure 15b are also present in this sample, and can be observed in areas of region P6 closer to the P6-P7 interface, and in region P7. The formations are larger and more dispersed, causing more of the substrate to be exposed, in P6 as compared to P7. The P7 region has agglomerations of Ni along the interface closest to the gap between regions P6 and P7. The rest of the P7 region has smaller and less dispersed agglomerations of Ni that are in a similar line-like formation as observed in P6.

Figure 15d is a micrograph of a sequence B sample (Ni deposited over Au) after annealing at 545 ^{o}C. In the P1 region, areas of darker and brighter contrast can be observed, as well as some areas with black contrast, indicating presence of Ni and Au, and small holes, respectively.

Region P2 has a darker contrast than P1 but more uniform morphology. There are also holes of varying sizes present; the smaller ones are along the P1-P2 interface, while the larger ones are closer to the opposite interface of the region. The largest hole is approximately 25 µm across the width of the region and is surrounded by much smaller holes along the P2-P3 interface border. In the P3 region, Au and Ni have agglomerated into small areas while maintaining the continuity of the film in the region. In contrast to P3, the P4 region appears brighter overall with large agglomerates of Au. Region P5 is dominated by large Au agglomerations with a film of mostly bright contrast and some darker contrast underneath, indicating presence of Au and Ni. The P6 region is comprised of small agglomerated islands of Ni and the Si substrate. The P7 region shows larger and more dispersed islands of Ni as compared to those in P6.

In region P1 of Figure 15e, small areas of dark and bright contrast represent a mixed morphology of Au and Ni. In comparison, the P2 region appears darker and has holes dispersed across the region. The interface between the P2 and P3 regions is characterized by a dark line indicative of the Si substrate. In the P3 region, Au and Ni have locally agglomerated while maintaining the continuity of the film in the region. In contrast to P3, the P4 region appears brighter overall with some large agglomerates of Au. Region P5 is dominated by large Au agglomerations with a film of mostly bright and some dark contrast underneath, indicating presence of Au and Ni. The P6 region is comprised of small agglomerated islands of Ni and the Si substrate visible underneath. The area of the P6 region closest to the P5-P6 interface shows smaller agglomerated islands of Ni which gradually increase in size throughout the region. There is a large divide between the P6 and P7 regions, which consists of intensities representing only the substrate. The border of the P7 region along the P6-P7 interface is lined with large

agglomerations of Ni continuous along the border. The P7 region consists of discontinuous, small line-like formations similar to those observed in the same region of Figure 15b stretching from the edge of the substrate wafer to the center.

Figure 15f shows the micrograph of the sequence B (Ni deposited over Au) sample after annealing at 730 ^{o}C. In region P1, large areas that are darker and brighter can be observed, as well as localized differences in contrast, indicating presence of Ni and Au, respectively. The area of the P2 region is darker, indicating more Ni content, and has some small holes present, indicated by spots of black contrast. The interface between the P2 and P3 regions is characterized by a dark line indicative of the Si substrate. In the P3 region, Au and Ni have uniformly agglomerated into small areas while maintaining the continuity of the film in the region. Region P4 appears brighter in comparison to P3 and has some large agglomerations of Au. Region P5 is dominated by large Au agglomerations with a film of mixed morphology underneath, indicating presence of Au and Ni. The area of the P6 region closest to the P5-P6 interface shows smaller agglomerated islands of Ni which gradually increase in size from one border of the region to the opposite border. There is a large divide between the P6 and P7 regions, which consists of intensities representing the Si substrate. The P7 region displays two distinct morphologies: (1) the line-like formations of Ni that extend from the edge of the substrate wafer towards the center, and (2) line-like formations of Ni that have curved and clustered into large areas, between which the substrate is visible as black contrast.

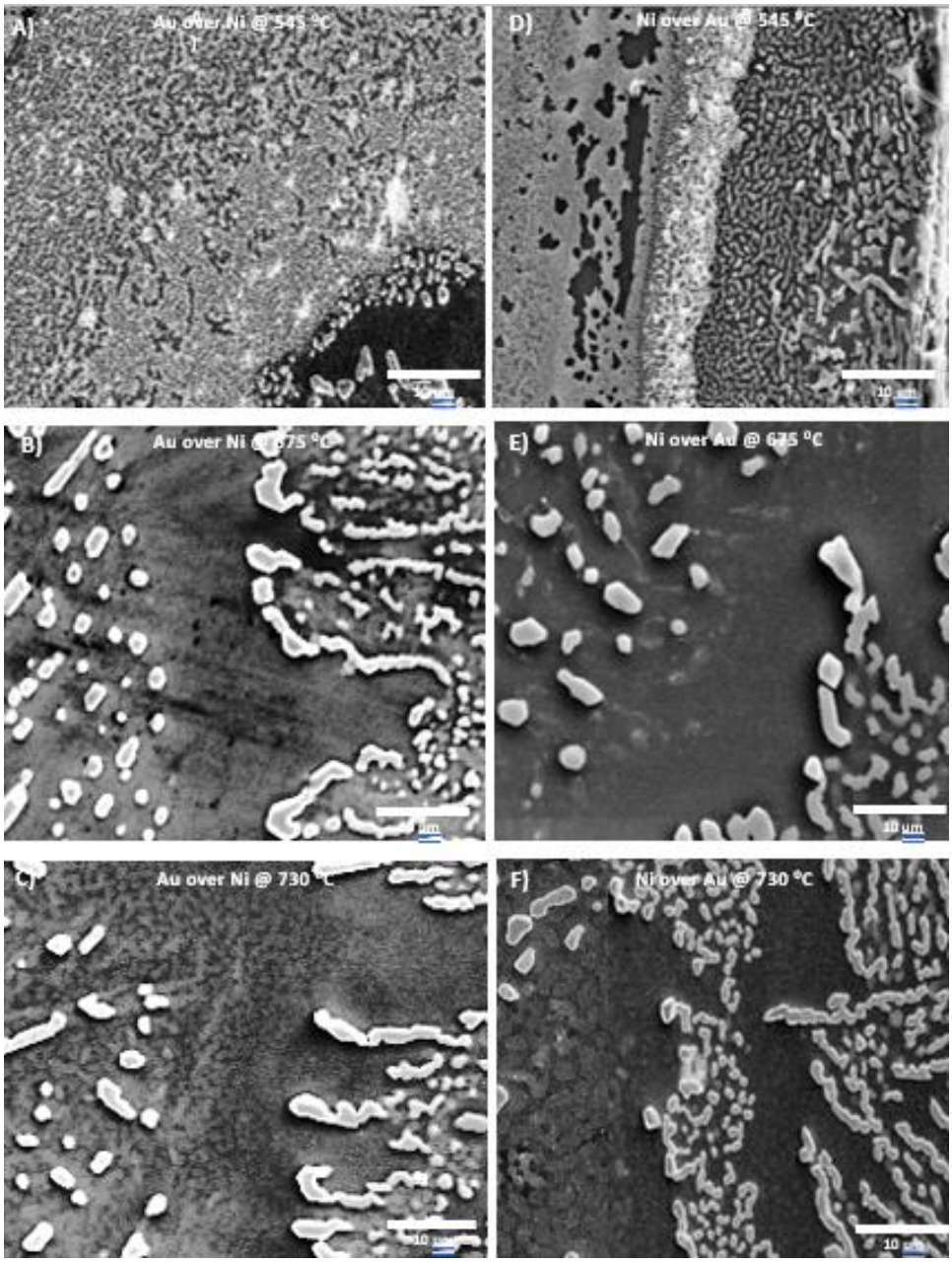

Figure 16 *: SEM micrographs of a) Au deposited on top of Ni and annealed at 545 ^{o}C b) Au deposited on top of Ni and annealed at 675 ^{o}C , c) Au deposited on top of Ni and annealed at 730 ^{o}C , d) Ni deposited on top of Au and annealed at 545 ^{o}C , e) Ni deposited on top of Au and annealed at 675 ^{o}C , f) Ni deposited on top of Au and annealed at 730 ^{o}C at a scale bar of 10 µm, comparing sizes of features in regions P6 and P7.*

Figure 16 shows SEM micrographs of the annealed metal bilayer films. The left column is comprised of samples of sequence A (Au deposited over Ni) while the right column shows images of sequence B (Ni deposited over Au). Bilayer films in a) and b) were annealed at 545 ^{o}C, those in c) and d) were annealed at 675 ^{o}C, and those in e) and f) were annealed at 730 ^{o}C. Figures 16b, c, e, f show features of regions P6 (left) and P7 (right). The figure serves to directly compare the areas and dimensions as all micrographs in the figure have ideal scale bar. While Figures 16a and 16d display relatively small regions P6 and P7 with small features that are similar in size. Figures 16b, c, e, f only show a section of the P6 and P7 regions with identical feature sizes. While the P6 region consistently has agglomerated islands of Ni that are widely dispersed, the P7 region characteristically has agglomerated islands of Ni that have formed line-like structures extending towards region P6 and spaced close to each other.

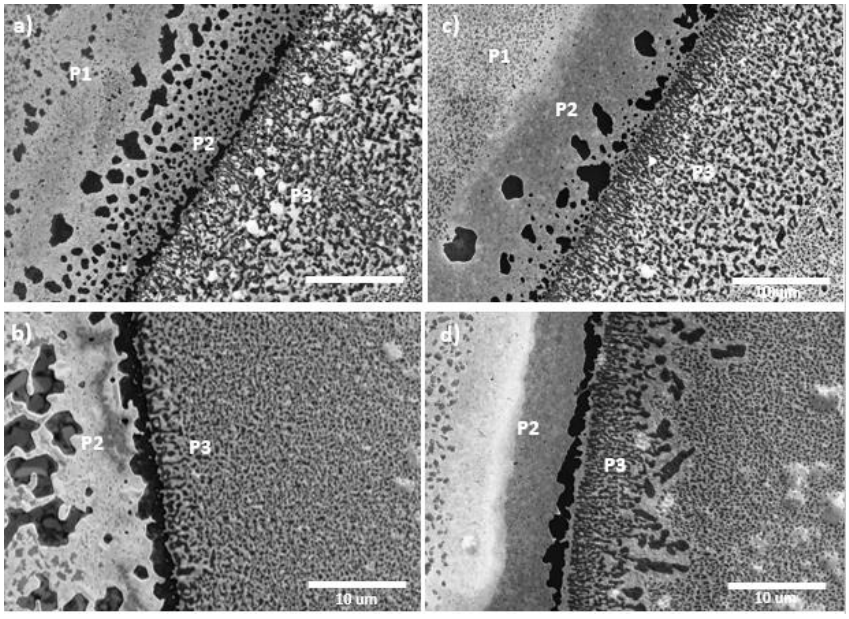

Figure 17 *: SEM micrographs of a) Au deposited on top of Ni and annealed at 675 ^{o}C b) Au deposited on top of Ni and annealed at 730 ^{o}C , c) Ni deposited on top of Au and annealed at 675 ^{o}C , d) Ni deposited on top of Au and annealed at 730 ^{o}C at a scale bar of 10 µm, detailing the morphology of both regions.*

Figure 17 shows SEM micrographs of the annealed metal bilayer films. The left column is comprised of samples of sequence A (Au deposited over Ni) while the right column shows images of sequence B (Ni deposited over Au. Figures 17a-d show features of regions P2 (left) and P3 (right). The figure serves to directly compare the relative widths of the regions and the sizes of morphological features. In Figures 17a and c, region 2 has relatively large holes approximately 2 μm in diameter close to the P1-P2 interface and small holes that are less than 500 nm along the P2-P3 interface. There is a gap characterized by a dark contrast between the P2 and P3 regions in all micrographs that is representative of the Si substrate. The P3 region grains of darker contrast stretching from the gap towards the P4 region. While the grains in the sequence A samples (Figures 17a and c) are relatively small, those in sequence B samples are as long as 5 to 10 μm.

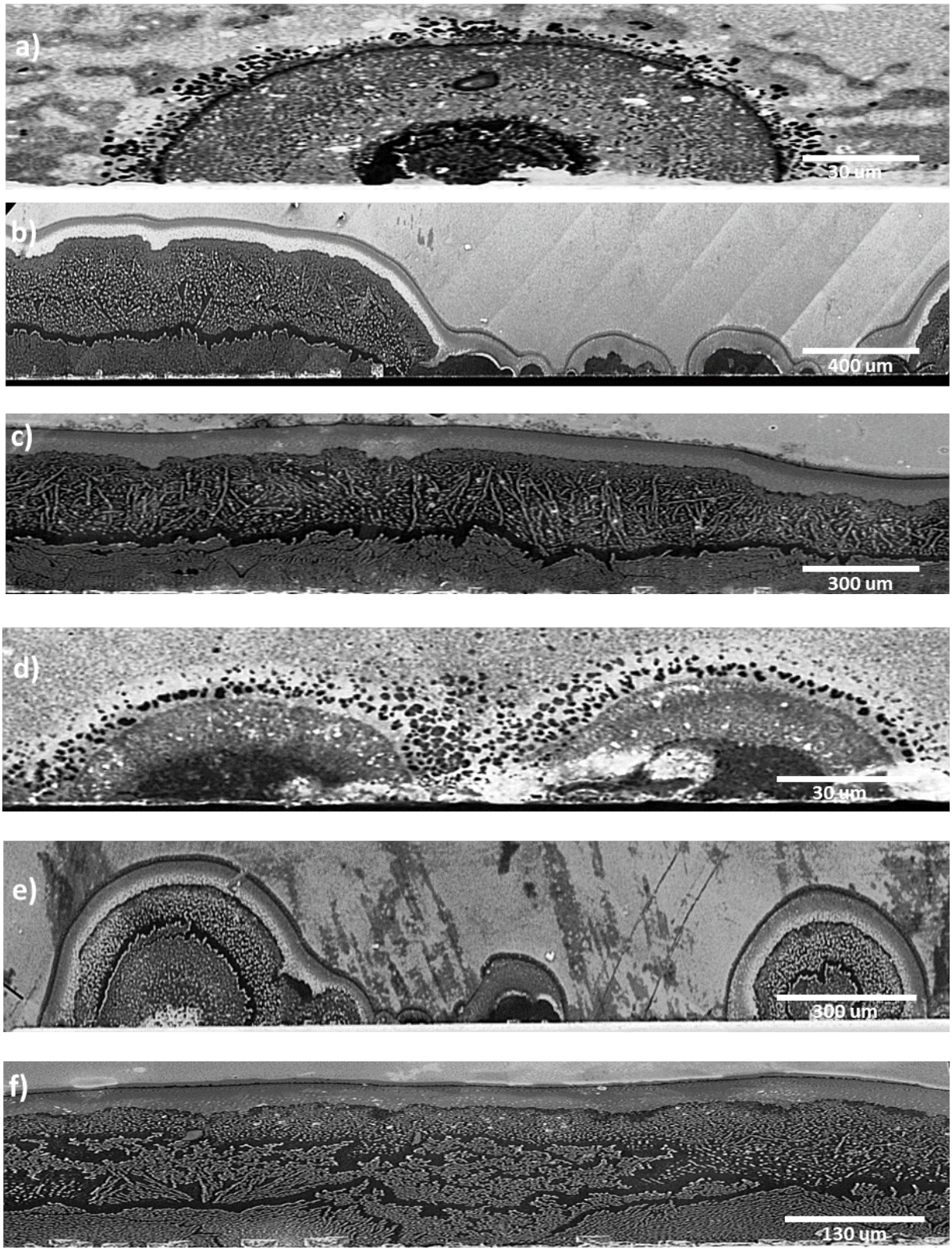
a)
30 um
b)
400 um
c)
300 um
d)
30 um
e)
300 um
f)
130 um

Figure 18: *MAPS of all the samples used in this study; a) is Au deposited on top of Ni and annealed at 545 ^{o}C b) is Au deposited on top of Ni and annealed at 675 ^{o}C, c) is Au deposited on top of Ni and annealed at 730 ^{o}C, d) is Ni deposited on top of Au and annealed at 545 ^{o}C, e) is Ni deposited on top of Au and annealed at 675 ^{o}C, f) is Ni deposited on top of Au and annealed at 730 ^{o}C.*

Figure 18 consists of large field of view images (MAPS) of all six samples which were used to determine borders between regions P2 and P3, P5 and P6, and sections of P7. Figure 18a shows a MAP of sequence A (Au over Ni) after annealing at 545 ^{o}C. A semi-circular area consisting of different regions with distinct morphologies is observed in the micrograph, indicating a single area where long-range edge retraction occurred. The relative widths of each region can be qualitatively compared to other regions and with regions of other samples. The retraction width in Figure 18a is an order of magnitude smaller as compared to the other samples of sequence A (see Table 1a). In addition, regions P1-P5 are larger in comparison to regions P6 and P7. Due to this, the curvature values from the P7 region are more difficult to extract. The semicircular appearance of the retracted area results in a high curvature ratio. Figure 18b is a micrograph displaying several areas where edge retraction has occurred. However, some regions of retraction are difficult to distinguish at this length scale due to the small size of their features, Figure 18c, on the other hand, shows a larger and continuous retracted area, with each individual region clearly distinguishable and the features that were observed in the previous figures for each region are present across the entirety of the sample. Due to the similar features observed in the 675 ^{o}C and the 730 ^{o}C samples, the curvature ratios in each of these regions are similar (see Table 1a).

Figures 18d to 18f display MAPs recorded from samples of sequence B after annealing at 545 ^{o}C, 675 ^{o}C, and 730 ^{o}C, respectively. As was observed for Figure 18a, Figure 13d has a retracted less compared to annealing at higher temperatures. The regions displayed are difficult to distinguish as compared to the other two samples, especially the P6 and P7 regions, due to the magnification. Unlike in Figure 18a, retraction of the film can be observed in two areas of the micrograph. This is indicative of the limited temperature dependence of edge retraction. Figure 18e shows the sample annealed at 675 ^{o}C with multiples areas where edge retraction is observed. However, one area has retracted further than the others, which are relatively small and do not have distinguishable features or regions. Figure 18f shows retraction occurring across the entire area of the sample in the micrograph. Each of the individual regions are clearly distinguishable and the film has retracted the furthest in this sample as compared to the others for sequence B (see Table 1b).

4.2 Image Analysis

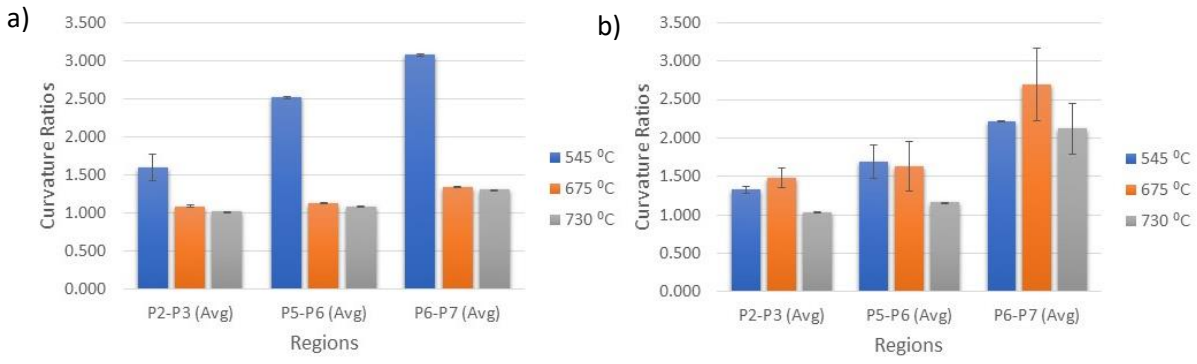

Figure 19: *Graphs of curvature ratios with error bars for a) Au deposited over Ni at all three temperatures, and b) Ni deposited over Au at all three temperatures.*

Figure 19 displays curvature ratios obtained from samples of sequence A (Au over Ni, Figure 19a) and sequence B (Ni over Au, Figure 14b). The blue, orange, and grey colors represent samples annealed at 545 ^{o}C, 675 ^{o}C, and 730 ^{o}C, respectively. For each sample, curvature ratios for borders P2-P3, P5-P6, and P6-P7 were determined. For sequence A samples annealed at 545 ^{o}C reveal the largest curvature for all regions, which drops significantly at 675 ^{o}C, but decreases only marginally upon heating to higher temperature. At low temperature (545 ^{o}C), P2-P3 interface shows the smallest curvature, followed by P5-P6 and P6-P7. At higher temperature, curvatures do not change.

a)

Regions	545 °C	675 °C	730 °C
P2	12.12 ± 3.23 (15.8%)	6.55 ± 1.26 (1.6%)	12.93 ± 2.45 (3.2%)
P3	1.89 ± 0.91 (2.5%)	4.63 ± 2.33 (1.1%)	5.85 ± 3.64 (1.4%)
P4	28.92 ± 6.41 (37.6%)	15.39 ± 4.21 (3.7%)	29.09 ± 8.11 (7.2%)
P5	23.22 ± 4.05 (30.2%)	35.39 ± 7.68 (8.5%)	40.68 ± 13.69 (10.0%)
P6	4.35 ± 1.27 (5.7%)	232.31 ± 24.73 (55.7%)	198.88 ± 33.54 (49.1%)
P7	6.41 ± 0.54 (8.3%)	123.08 ± 20.65 (29.5%)	117.52 ± 27.81 (29.0%)
Total	76.91 ± 13.36	417.35 ± 56.31	404.95 ± 63.45

b)

Regions	545 °C	675 °C	730 °C
P2	13.24 ± 4.67 (26.2%)	11.21 ± 2.78 (4.6%)	7.14 ± 2.65 (2.1%)
P3	0.78 ± 0.22 (5.7%)	3.25 ± 0.89 (1.3%)	3.95 ± 1.27 (1.1%)
P4	1.73 ± 0.91 (18.0%)	24.81 ± 5.23 (10.2%)	22.07 ± 3.93 (6.4%)
P5	5.12 ± 2.43 (9.2%)	15.37 ± 5.72 (6.3%)	23.38 ± 6.02 (6.7%)
P6	13.08 ± 3.11 (22.4%)	56.51 ± 9.40 (23.2%)	78.56 ± 16.53 (22.7%)
P7	12.11 ± 3.27 (18.5%)	132.23 ± 17.78 (54.3%)	211.65 ± 23.38 (61.0%)
Total	46.05 ± 11.36	243.38 ± 47.54	346.76 ± 53.64

Table 1: *Absolute and percentage of total widths values of regions P2 to P7 at each of the three temperatures in µm for a) Au over Ni (Seq. A) and b) Ni over Au (Seq. B).*

Table 1a details the absolute width and percentage of total width for each region (P2 to P7) for all three samples of sequence A while 1b offers the same data for sequence B. Tables 1a and 1b reveal the general trend that the total width of each area of retraction is increasing with the annealing temperatures. Table 1a shows the width values of samples at 545 ^{o}C and 730 ^{o}C are similar for regions P2 to P4, after which the 730 ^{o}C sample breaks trend with a wider P5 region as compared to the 545 ^{o}C sample. In contrast, though the width of the P3 region is similar in the 675 ^{o}C and the 730 ^{o}C samples, the widths of other regions of the 675 ^{o}C sample are not in the same range as those of the other two. The width of regions P6 and P7 is significantly less in 545 ^{o}C sample as compared to the other two. The 675 ^{o}C and the 730 ^{o}C samples have much wider P6 regions as compared to P7 regions. In Table 1b, while the P2 regions of all three samples are similar in width, only the 675 ^{o}C and the 730 ^{o}C samples have similar widths for regions P3 to P6, while the width of each region in the 545 ^{o}C sample is drastically smaller in comparison. Furthermore, after annealing at 730 ^{o}C, the P4 and P5 regions remain similar in width, while in the 675 ^{o}C sample, the P5 region decreases in width as compared to the P4 region. The P7 region for the 730 ^{o}C sample is almost twice the width of the region after annealing at 675 ^{o}C. Both samples display the trend of having a larger P7 region as compared to the P6 region.

The percentage values in Table 1 allow direct comparison of the samples to each other. Table 1a compares the P4 and P5 regions of the 545 ^{o}C sample to the P6 and P7 regions of the other two samples, respectively. The P6 region of 675 ^{o}C sample is similar in percentage to the P6

region of 730 ^{o}C sample, and the same trend is observed in the P7 region of the same samples. The P4 and P5 regions of the 545 ^{o}C sample show a similar trend as observed in the 730 ^{o}C sample. Table 1b determines that the percentage values of the P6 region across all three samples are similar, while the P7 regions account for more than half of the retracted area of the 675 ^{o}C and 730 ^{o}C samples. The P7 region of the 545 ^{o}C sample does not follow that trend and slightly decreases in value compared to the P6 region. A consistent observation across the percentages for both sequences is that the P2 region of the 545 ^{o}C sample for both sequences is significantly larger than the P2 region for the other two samples of each sequence.

4.3 Spectroscopy

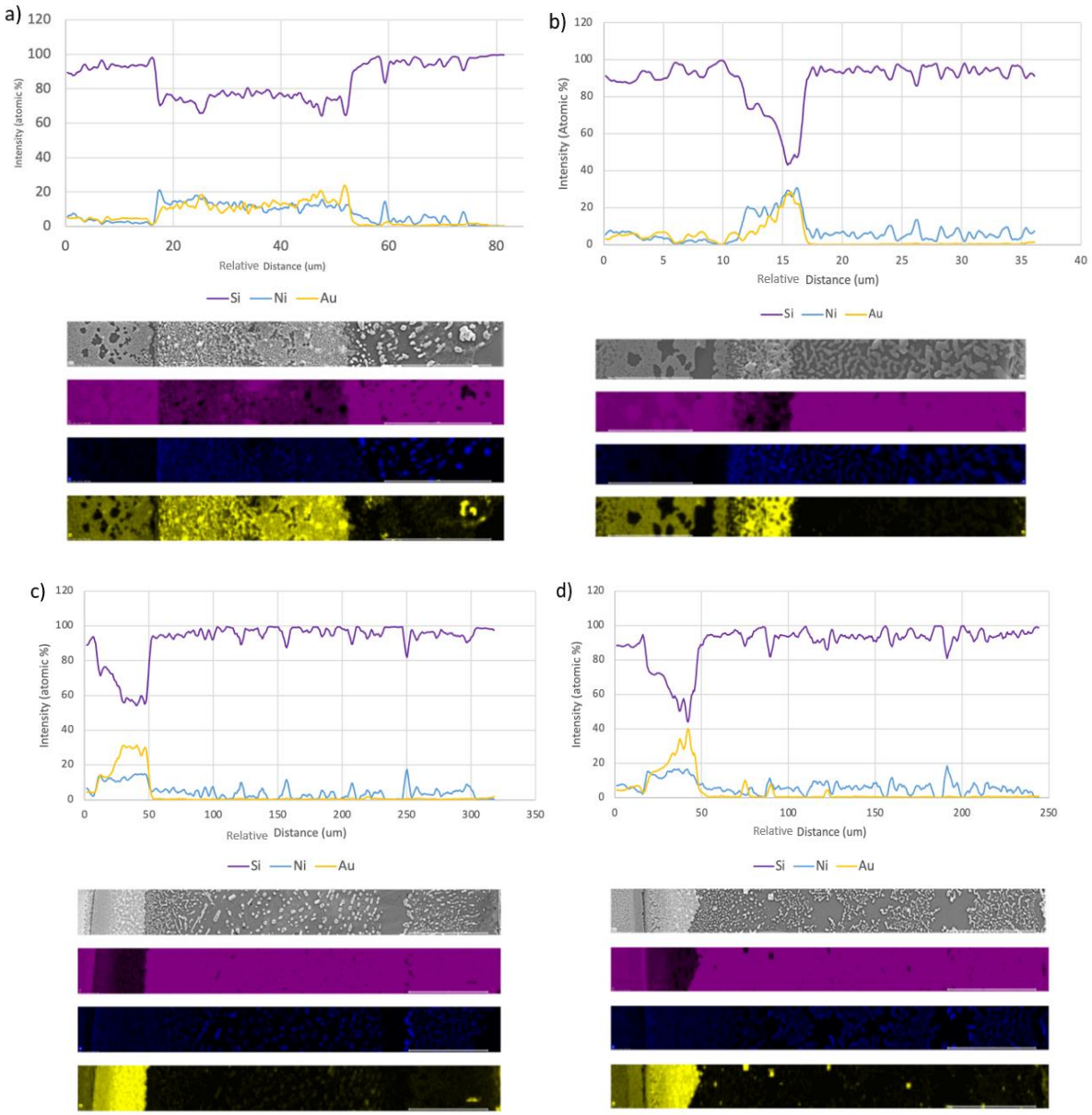
a)
Intensity (atomic %)
Relative Distance (um)
Si Ni Au
b)
Intensity (Atomic %)
Relative Distance (um)
Si Ni Au
c)
Intensity (atomic %)
Relative Distance (um)
Si Ni Au
d)
Intensity (atomic %)
Relative Distance (um)
Si Ni Au

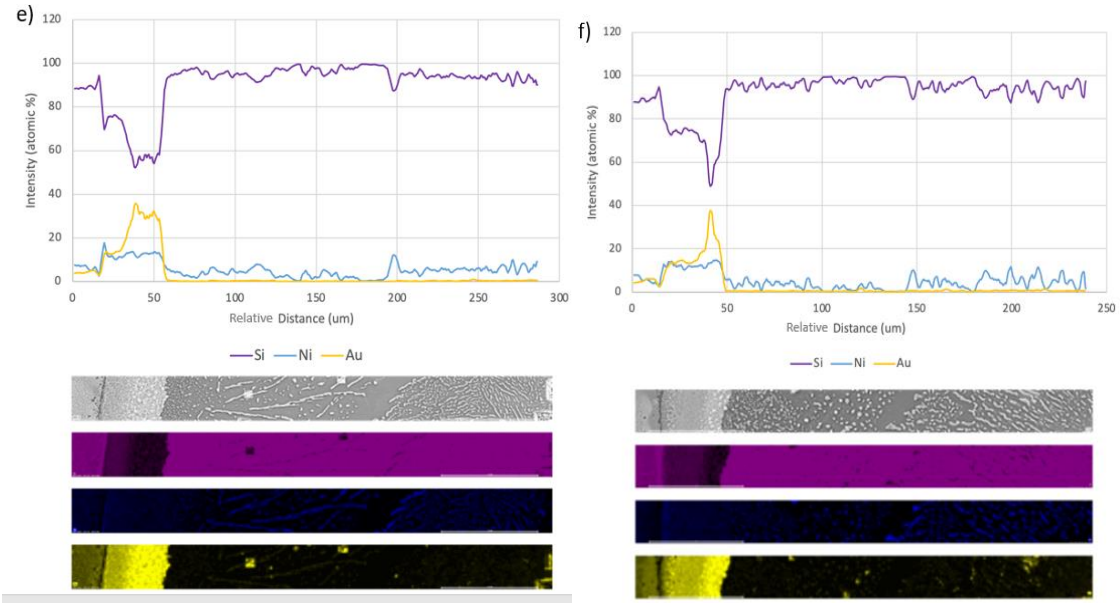

Figure 20: *Elemental intensity versus distance graphs and SEM/EDX images for all of the samples used in this study; a) is Au deposited on top of Ni and annealed at 545 ^{o}C b) is Ni deposited on top of Au and annealed at 545 ^{o}C, c) is Au deposited on top of Ni and annealed at 675 ^{o}C, d) is Ni deposited on top of Au and annealed at 675 ^{o}C, e) is Au deposited on top of Ni and annealed at 730 ^{o}C, f) is Ni deposited on top of Au and annealed at 730 ^{o}C.*

Figure 20 shows integrated EDX intensities as a function of distance with corresponding SEM survey images and EDX chemical distribution maps. In Figures 20a and 20b, both Au and Ni start at 0 µm at a relatively low intensity, which is recognized as the P1 region. The intensity of each element is 0 mol % in the interface between regions P2 and P3, indicating an absence of both metals. The intensity of Ni increases sharply at the border of region P3, drops slightly and stays at that intensity throughout regions P3 to P5. The intensity of Au increases more steadily in the P3 region and remains at the same intensity as Ni throughout regions P3 to P5. At the border of region P5, the intensity of Ni decreases gradually, while that of Au drops sharply to 0 mol %. While there are fluctuations of Ni in the P6 and P7 regions, Au remains at 0 mol % intensity. The

absolute distance of regions P3 to P5 in Figure 20a is significantly larger than in Figure 20b, while that of the other regions is in the same range, indicating that the sequence A has retracted more than sequence B at 545 ^{o}C.

Regions P3 to P5 in Figures 20c to 20f have an Ni intensity that is approximately half of the maximum intensity of Au. In all sequence B (Ni/Au) samples, intensity of Au in regions P3 to P5 increases steadily, with a maximum intensity in the P5 region before dropping sharply to 0 mol %. In all sequence A samples, the intensity of Au increases quickly throughout the P3 and P4 regions and stays at the maximum value in region P5 region before dropping sharply to 0%. In the P3 region of all 675 ^{o}C and 730 ^{o}C samples, Au and Ni are consistently observed to be at the same intensity levels, with Au only starting to increase in the P4 region. There is also a sharp Ni peak observed at the beginning of the P7 region, which is visible more clearly in the EDX image that displays only Ni. While there is no Au observed in the P6 and P7 regions, there are some agglomerations of Au detected in those regions in Figure 20d. They can also be observed in the EDX maps that displays Au.

5. Discussion

5.1 The role of NiO_x in long-range edge retraction

After annealing, all six samples exhibited long-range edge retraction and localized dewetting. The same observed in this study reproduce a previous study by Cen et al for Au/Ni bilayer films annealed at 675 ^{o}C. However, that study had an additional NiO_x layer between the Ni layer and Au layers from breaking vacuum between deposition of the two metal films [10]. Therefore, both studies can be directly compared to explore the differences observed as a result of the additional NiO_x layer. Cen et al established that regions P2 and P3 were Au and Ni-rich regions, respectively. While a large agglomeration of Au was observed in regions P4 and P5, Ni decreased sharply in region P3 and continued to steadily decline throughout regions P4 to P7. Region P6 showed a dewetting of the continuous film, with some large agglomerations of Ni and region P7 had some small agglomerations of Ni. In this study, Figure 20b shows that region P2 is Au-rich in comparison to the amount of Ni present, but there is not a significant concentration of Au present as compared to the concentrations in the P1 region. Region P3 is Ni-rich but the concentration of Ni remains at the same level throughout regions P4 and P5. There are also significant amounts of Ni found in the P6 and P7 regions, with line-like formations of Ni present in both. The total retraction distance reported by Cen et al is approximately half of the retraction distance observed in this study, indicating that the presence of a NiO_x layer decreases the rate of retraction. The same trend is observed to a lesser extent when comparing retraction distances between sequences A and B at all temperatures, suggesting that temperature and presence of the NiO_x layer are both factors that affect

retraction distance. The NiO_x layer is reduced when heated at high temperatures under atmospheric conditions [40]. The reported activation energy for the reduction of NiO_x is 85.6 kJ/mol [41], with other studies yielding values as low as 53.5 kJ/mol and as high as 96.4 kJ/mol [42-44]. Since the calculated activation energies of the farthest retracted regions, P6 and P7, are higher than or in the range of those for the reduction of NiO_x (see Figure 17), a reasonable assumption is that NiO_x reduction occurred in those regions while annealing and was enough to facilitate retraction. Based on retraction distance (see Table 1), sequence A samples retract the fastest, then sequence B samples, and samples studied by Cen et al, which are the slowest [10]. The reason this occurs is partially due to the presence of the NiO_x layer, or lack of. The diffusivity of Au is higher than that of Ni, suggesting it retracts faster than Ni. Sequence A samples lack an NiO_x layer. Sequence B samples are assumed to have an NiO_x layer, due to the exposure of the Ni layer to atmosphere, which restricts the retraction of the Ni and Au layers due to the lack of a free surface. The samples used by Cen et al had an NiO_x layer between the Au and Ni layer, allowing the Au layer a free surface to retract but hindering the retraction of the Ni layer and causing local dewetting [10]. The slower retraction rate for Cen et al samples compared to the sequence B samples indicates that the diffusion mechanisms by which retraction occurs require the interaction of the Au and Ni layers. Furthermore, the calculated activation energy for the P7 region in sequence B samples is similar to that of the sequence A samples despite the additional NiO_x layer. The study by Cen et al also reported that the Au/SiO_2 interface was more favorable than the Ni/SiO_2 interface [10]. A hypothesis is the activation energy of sequence B samples would be less than that for sequence A samples in the absence of the NiO_x layer, indicating that the deposition sequence affects the occurrence of long-range

edge retraction, and Ni having a free surface and an Au/SiO_2 interface is more favorable for retraction than Au having a free surface and an Ni/SiO_2 interface. A cross-sectional TEM study is required of sequence B samples not exposed to the atmosphere to confirm this hypothesis but is outside the scope of this study.

5.2 Mechanisms of long-range edge retraction

During long-range edge retraction, the bilayer film displays areas of varying morphologies (i.e. P1 through P7 regions). These regions are present in all bilayer film samples (see Figure 20) and have similar characteristics per region with some differences based on deposition sequence. This indicates that they have distinct underlying mechanisms by which each region forms in each of the deposition sequences. In an attempt to identify the governing mechanisms, activation energies for each region were determined from the observed widths of each region listed in Table 1 using the Arrhenius relation:

$$k = A\, e^{-Ea/RT} \qquad \text{(Equation 6)}$$

K is the rate constant, which is the rate of a chemical reaction, A is the frequency factor while denotes the frequency of molecules that collide in the correct orientation and with enough energy to initiate a reaction, R is the gas constant, T is the temperature, and E_a is the activation energy. The activation energy was calculated for region P3 to P7 for both deposition sequences.

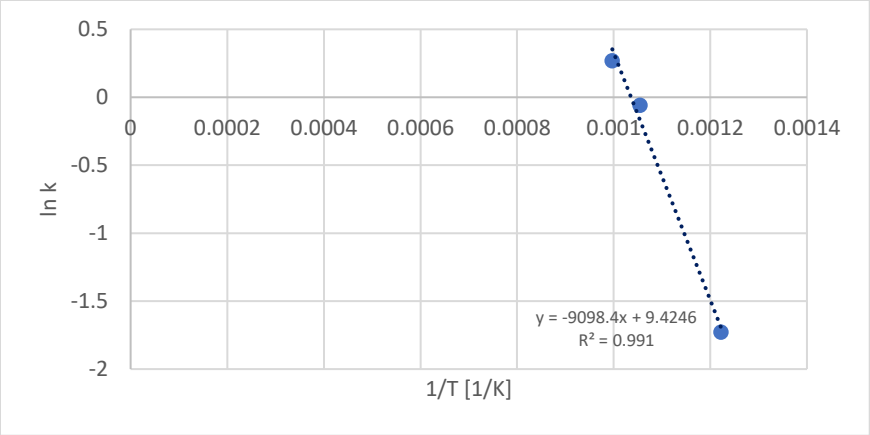

Figure 21: *A 1/T versus ln k representative graph used to determine E_a from the slope in the equation of the dotted line plotted. The graph was used to determine E_a of the P6 region of sequence B samples.*

The slope of Figure 21 was used to calculate the E_a with the relation slope = $\frac{-Ea}{R}$ for regions P3 to P7 of both sequences, as shown in Figure 22.

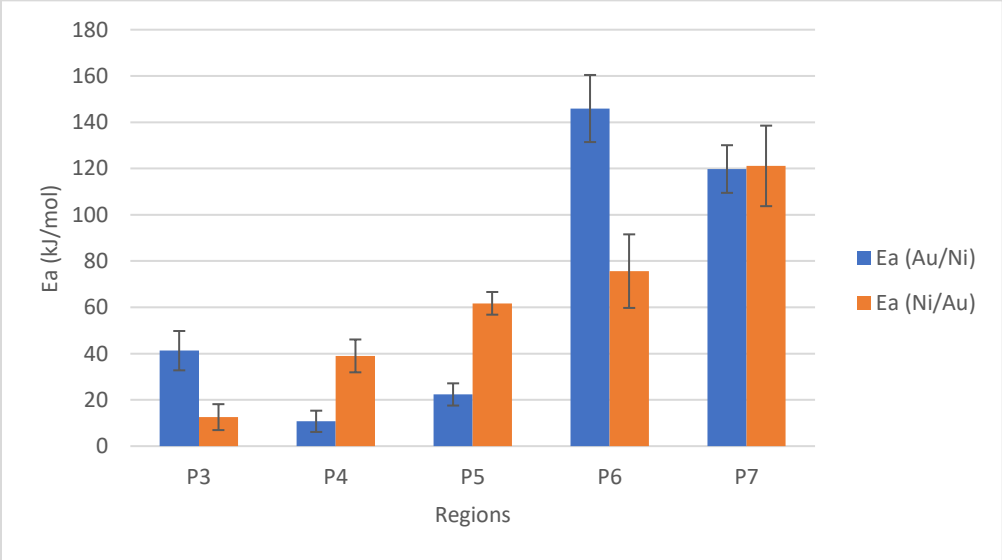

Figure 22: *The activation energies determined from the width measurements for each region (P2-P7). The blue bar shows the activation energy for sequence A samples, and the orange bar shows the activation energy for sequence B samples.*

Figure 22 shows the resulting activation energies in units of kJ/mol. The blue bars represent the activation energies for sequence A (Au over Ni), while the orange bars represent the activation energies for sequence B (Ni over Au). An activation energy represents the energy required for a mechanism that drives retraction in a specific region. An increasing trend in the activation energy of sequence B, from P3 to P7 can be observed. There is no clear trend that can be observed for sequence A, however.

a)

Diffusion Mechanisms	E_a in kJ/mol
Surface Diffusion of Au in Au	38.59
Interface Diffusion of Au in Au	84.91
Volume Diffusion of Au in Au	174.47
Surface Diffusion of Au in Ni	49.21
Interface Diffusion of Au in Ni	Range of 40 to 60
Volume Diffusion of Au in Ni	119.6
Surface Diffusion of Ni in Ni	86.11
Interface Diffusion of Ni in Ni	114.6
Volume Diffusion of Ni in Ni	292
Surface Diffusion of Ni in Au	49.21
Interface Diffusion of Ni in Au	90.7
Volume Diffusion of Ni in Au	173.7

b)

Regions	Sequence A: Ea (kJ/mol)	Possible Mechanism(s)	Sequence B: Ea (kJ/mol)	Possible Mechanism(s)
P3	41.27 ± 8.53	Surface Diffusion of Au in Au Surface Diffusion of Au in Ni Surface Diffusion of Ni in Au	12.54 ± 5.66	-
P4	10.73 ± 4.61	-	39.00 ± 7.14	Surface diffusion of Au in Ni Surface diffusion of Ni in Au Surface diffusion of Au in Au
P5	22.33 ± 4.82	-	61.73 ± 4.94	Interface Diffusion of Au in Ni
P6	145.93 ± 14.51	Volume Diffusion of Au in Au Volume Diffusion of Ni in Au	75.64 ± 15.93	Interface Diffusion of Au in Ni Surface diffusion of Ni in Ni Interface Diffusion of Ni in Au
P7	119.77 ± 10.33	Volume Diffusion of Au in Ni Interface Diffusion of Ni in Ni	121.13 ± 17.41	Volume Diffusion of Au in Ni Interface Diffusion of Ni in Ni

Table 2: *a) Diffusion mechanisms and corresponding activation energies as reported in literature [45-55] and b) the calculated activation energies in kJ/mol with error bars for regions P3 to P7 for sequences A and B, and the possible mechanisms that correspond to those energies.*

While there may be multiple mechanisms contributing to edge retraction in each of the regions, a reasonable assumption can be made that the calculated activation energies of each region is indicative of the dominant mechanism responsible for retraction in the region. For both sequences, the activation energy of the region P7 is very similar to the reported activation energy of volume diffusion of Au in Ni and interface diffusion of Ni in Ni in literature, as seen in Table 2. For sequence A, the dominant mechanism is likely interface diffusion of Ni in Ni. Since Au has a free surface, surface diffusion of Au in Au is more energetically favorable as compared to volume diffusion of Au in Ni. Furthermore, the Ni layer does not have a free surface, so the most energetically favorable mechanism is interface diffusion of Ni in Ni. While sequence B has

a similar activation energy as sequence A, the dominant mechanism is volume diffusion of Au in Ni, the reason being that the Ni layer has a free surface after the reduction of NiO_x presumed to have accumulated on the surface. As such, surface diffusion of Ni in Ni is more energetically favorable to interface diffusion of Ni in Ni. Additionally, the Au layer does not have a free surface and volume diffusion of Au in Ni is more energetically favorable than volume diffusion of Au in Au.

In region P6, the activation energy for sequence A increased while that for sequence B decreased. The activation energy for sequence A corresponds to the literature value for volume diffusion of Au in Au and Ni in Au while the one for sequence B corresponds to interface diffusion of Au in Ni and Ni in Au and surface diffusion of Ni in Ni. For sequence A, volume diffusion of Au in Au is likely the dominant mechanism of edge retraction, evidenced by the presence of Ni and the absence of Au in the P6 region. Since Au has retracted completely from region P6, it can be inferred that the dominant mechanism must be one that facilitates the retraction of Au. For sequence B, interface diffusion of Au in Ni is the likely mechanism that dominates in region 6. While Au diffused through the bulk Ni layer in region P7 due to not having a free surface, the breakup of the Ni layer in the P6 region makes interface diffusion of Au in Ni more favorable. Additionally, Au is absent from the P6 region and interface diffusion of Au in Ni is the only mechanism which facilitates the retraction of Au from the region and has a lower reported activation energy than the one calculated.

While there are no activation energies of mechanisms in literature that match the activation energies of the regions P4 and P5 of sequence A. However, region P3 of sequence A has three possible mechanisms that the calculated activation energy can be attributed to. Surface

diffusion of Au in Ni and of Ni in Au have the same reported activation energies in literature but surface diffusion of Ni in Au is dominant in this region, as observed from the higher concentration Ni in Figures 20a, c, and e. For sequence B, the calculated activation energy of the P3 region does not have a corresponding value from literature. However, there are corresponding activation energies for the P4 and P5 regions. In region P5, the dominant mechanism is interface diffusion of Au in Ni. The EDX maps in Figures 20b, d, and f show agglomerates of Au near the P5-P6 interface in the P5 region, along with a peak in concentration of Au in the same area and a steady drop from regions P5 to P3. The peak appears sharper as annealing temperature increases indicating that Au does retract as far at higher temperatures as compared to lower temperatures. A reason for this is alloying occurs at high temperatures [56] and restricts the size of the grain boundaries to, effectively limiting interface diffusion of Au in Ni. The dominant mechanism in region P4 is surface diffusion of Ni in Au, since the Ni layer is atop the Au layer but more Au is present in the region as compared to Ni (see Figures 20b, d, and f).

5.3 Corner and Fingering Instabilities

Long-range edge retraction has been observed in bilayer films annealed at three different temperatures. Figure 18 shows micrographs of the retracted areas. Each area of retraction propagates in the shape of a semi-circle. The semi-circular formation and propagation of retraction is characteristic of a corner instability. A corner instability originates from nucleation points along the edge of the substrate. In this study, those points are structural defects that can

be observed along the edge of the substrate (see Figure 18a). The semi-circular formation is evident in Figures 18a, b, d, and e. One or multiple areas of retraction can be observed, but the formation is not observed in samples annealed at 730 °C (Figures 18c and f). This can be explained by the faster merging of several corner instabilities at higher temperature. Areas observed in Figures 18c and f are considered a result of multiple corner instabilities that have merged. The curvature ratios shown in Figure 19 were calculated by measuring each of the three interfaces listed parallel to the triple line (see Figure 15). For sequence A samples, the highest curvature ratio was observed after annealing at 545 °C since insufficient thermal energy was available to farther retract. For sequence B, however, the highest curvature ratio was observed after annealing at 675 °C. The reason for this is that the retraction of sequence B is hindered by the presence of the native NiO_x. This indicates that the corner instability has a lower temperature limit that determines if it will take place.

In regions P6 and P7 after annealing at 675 °C or 730 °C, line-like formations (see Figures 15b, c, e, f) are observed oriented from the edge of the substrate towards the center (region P1). Their morphological features are characterized by their high aspect ratios, typically of fingering instabilities [7]. They form as an effect of the receding edge (see P5-P6 and P6-P7 interfaces in Figure 19). Interfaces of positive curvature are fingers and spacings between them that vary. Figure 19 shows that the P6-P7 interface has the highest curvature, indicating that curvature of features increases inversely with size of those features. An explanation for this is smaller structures are energetically unstable and become stable by agglomerating with other structures or increasing their curvature.

5.4 Pinch-off events and void nucleation

Regions P2 and P3 were found to be Au and Ni-rich, respectively (see Figure 20) while region P2 is only Au-rich for sequence B samples (see Figures 20b, d, f). Au is present in region P2 of sequence A samples but it is not as concentrated as for sequence B. Abrupt interfaces between regions P2 and P3 are observed. Figures 16a and 16d show grains of Ni oriented towards regions P4 and P5, indicating the diffusion of Ni from P2 to P3. The diffusion of Ni is a result of the large chemical potential present due to the agglomeration of Au in P4 and P5 [10]. There are two possible mechanisms that may be occurring to cause the interface between regions P2 and P3. Figures 16b and 16d have large and small holes that have formed in the P2 region. Ni diffusing to region P3 from P2 leads to the thinning of region P2. As a result, voids that form at the Ni/Au interface [59] can nucleate to the surface with relative ease as compared to other regions. As the voids combine in the interface between regions P2 and P3 across the retracted area, they form a continuous gap that is devoid of Au and Ni. Another possible mechanism is a pinch-off event occurring in regions P3 to P5 and as a result, forming a gap (i.e. P2-P3 interface). A pinch off event occurs at a point where a valley forms in the film that is deep enough to expose the substrate surface. Defining characteristics of a pinch-off event are: (1) the valley must be preceded by a rim that is at least two times larger in height (i.e. h(x)) than the uniform film, (2) has a sufficient mean curvature of the rim ($\frac{1}{h(x)}$), which is a function of the equilibrium contact angle between the film and the substrate (Figure 2a), and (3) can develop in a specified amount of annealing time [60]. Pinch-off events have thus far only been suggested for monolayer films [7, 60]. Pinch-off events in a bilayer film may not display all the necessary

characteristics that are observed in monolayer films. In regions P4 and P5, the retracting edge deposits large concentrations of Au and Ni in the P4 and P5 regions (see Figure 20), which agglomerate and reach a critical height ($h(x)_c$; a height at which pinch-off can occur), causing a pinch-off event to occur. The critical height can be evaluated through a comparison between the concentration of the P1 region (uniform film) and the P5 region (the rim) as is discussed in Table 3 as a thickness ratio. The concentrations were derived from the concentration vs. relative distance graphs in Figure 20.

Samples (Annealed at T)	Ratio of Au (P5/P1)	Ratio of Ni (P5/P1)	Combined Ratio
Seq A (545 ^{o}C)	4.615	3.205	7.819
Seq B (545 ^{o}C)	4.952	3.532	8.483
Seq A (675 ^{o}C)	6.961	3.179	10.141
Seq B (675 ^{o}C)	9.146	2.570	11.717
Seq A (730 ^{o}C)	7.760	1.929	9.689
Seq B (730 ^{o}C)	7.927	1.788	9.705

***Table 3**: The ratio of concentration measured in region P5 in comparison to that measured in region P1 for Au and Ni, respectively, as well as a combined ratio determined by the addition of the Au and Ni ratios for each of the six samples.*

It is observed that the concentration ratios range from 1.79 to 11.72. The Ni ratios of sequence A samples are consistently higher, though by a decreasing margin as the annealing temperature increases. The ratio of Au is higher for sequence B samples at 675 ^{o}C and 730 ^{o}C, but not for the sample at 545 ^{o}C. Since even the lowest ratio denotes a rim height that is approximately two times larger than that of the uniform film, a pinch-off event may be occurring. While the rim

height is necessary to determine the occurrence of pinch-off, it is not sufficient. The equilibrium contact angle, and the reliant curvature of the rim and the annealing time required for pinch-off occurrence are important factors which cannot be evaluated based on available data. A cross-sectional TEM study is required to determine both factors but is outside the scope of this project.

6. Conclusion

Dewetting transitions and mechanisms of long-range edge retraction of Au/Ni bilayer thin films were investigated in this study. Au and Ni bilayer films were deposited in two distinct sequences consisting of Au layer deposited on top of an Ni layer on a SiO_2/Si substrate, and Ni layer deposited on top of an Au layer on a SiO_2/Si substrate. Samples underwent rapid thermal annealing in the same conditions at 545 °C, 675 °C, and 730 °C. Each sample was characterized through SEM and EDX studies to collect data on the morphological changes and chemical composition of the samples.

Each sample had undergone long-range edge retraction and displayed regions of agglomeration and retraction. Seven distinct regions observed in each sample. Each corresponding region displayed similar morphology across all samples. Au/Ni bilayer films annealed at 675 ^{o}C were directly compared to a previous study by Cen et al [10]. The study by Cen et al had an NiO_x layer between the Ni and Au layers that was absent in this study. In contrast to the previous study, there was no Au found in the P6 region of any of the samples in this study. In regions P3 to P5, an accumulation of Ni was present, which was also not observed in the previous study. A comparison of samples of both sequences reveals that sequence A samples have retracted further than sequence B samples and report larger P6 and P7 regions.

It was concluded that the presence of NiO_x, or the lack of it in sequence A, serves as the origin of the observed differences. In sequence B (Ni over Au), NiO_x is assumed to have accumulated on the surface of the Ni layer due to oxidation reactions, restricting the movement of the Ni and Au layers underneath due to the lack of a free surface. A high activation energy for

reduction of NiO_x denotes that the NiO_x layer has a stabilizing effect on the film. In addition, the study by Cen et al also reports a much smaller retraction distance as compared to both sequences annealed at 675 °C, indicating that the interaction of the Au and Ni layers is crucial to long-range edge retraction. Characterization of the Au/Ni bilayer films revealed seven distinct regions with different morphologies forming as the bilayer film retracted from the edge. A calculation of the activation energies based on Arrhenius analysis allowed the activation energies of regions P3 to P7 to be compared to literature values of possible mechanisms that drive edge retraction in each region. Regions P6 and P7 were found to have dominant mechanisms of interface and volume diffusion. Region P5 appeared to be a transition region with interface diffusion as the dominant mechanism, while regions P3 and P4 were formed by surface diffusion. Based on the observations made, interface diffusion is the dominant mechanism of edge retraction. The driving force of these mechanisms is the minimization of free excess surface energy due to capillarity.

Corner instability is a primary mechanism of long-range edge retraction and is observed as the retraction initiates at a straight edge and propagates into the film in a semi-circular shape. The mechanism balances two opposing effects: (1) the mass that is collected by the edge as it retracts increases the rim height, while (2) the increasing arc length as the instability progresses decreases the rim height [7]. The instability initiates at multiple points along the edge of the bilayer film due to structural defects or anisotropy, causing retraction to occur in several areas. Previously, the corner instability had only been observed in monolayer films retracting from a corner, i.e. a point at which two straight edges meet, however, this study establishes that a corner is not necessary to instigate the instability. Multiple retracted areas merge to form one

area of retraction, as indicated by the curvature ratio of P2-P3 interface. Line-like features observed in regions P6 and P7 of samples annealed at 675 ^{o}C and 730 ^{o}C are a result of a fingering instability as evidenced by the P5-P6 interface and the P6-P7 interface. Smaller features from P6-P7 interface have higher curvatures, establishing an inverse relationship between size and curvature. Small features are energetically unstable and agglomerate with other features to become stable. The P2-P3 interface is a result of void nucleation or of a pinch-off event. The diffusion of Ni from P2 to P3 caused a thinning of the region and allowed voids to nucleate to the surface. The combination of the voids in the region results in the abrupt interface. Edge retraction leads to accumulation of Au and Ni in regions P4 and P5, increasing the concentration to a critical height of the rim, leading to the formation of a valley: the P2-P3 interface. The consideration of the curvature of the rim is not available and is outside the scope of this study.

7. Future work

7.1 Ex-situ characterization of Au/Ni bilayer thin films

The material components for this study were selected due to the variability in results based on various conditions, such as deposition sequence, annealing temperature and the corresponding solubility of the metals. In this study, the results of various combinations of these conditions have been studied, such as three annealing temperatures and two deposition sequences. This study concludes that there are differences in the mechanisms that drive edge retraction of an Au/Ni bilayer film dependent on the deposition sequence. While the interactions between Au and Ni when only one has a free surface have been studied, it remains unclear how the interactions and the mechanisms of retraction would change when both have a free surface. To advance the study of the agglomeration and edge retraction in Au/Ni bilayer films, an additional deposition sequence of Au and Ni co-deposited on to a substrate and annealed under similar conditions can be studied to determine how the dominant mechanisms of retraction change between a homogeneous bilayer film and a heterogeneous monolayer film in which both Au and Ni have a free surface. The current study only explored the interactions of Au and Ni when it was energetically favorable but a co-deposited film will explore the interactions of both elements even when it is not energetically favorable. While this study compared the dynamics of edge retraction based on deposition sequence, the assumed oxidation of the Ni layer in sequence B due to exposure to atmospheric conditions made a direct comparison difficult. As such, the deposition and annealing of a sequence B sample under vacuum and without exposure to atmospheric conditions would serve to eliminate the effects of the NiO_x layer and

allow a direct comparison to be made with the sequence A samples of this study and reveal the mechanistic differences due to deposition sequence, and to determine the role of the NiO_x layer in edge retraction.

7.2 In-situ characterization of Au/Ni bilayer thin films

All previous work in this group has been conducted on samples of Au and Ni deposited in two different sequences and undergone rapid thermal annealing at three temperatures. All studies thus far have been ex-situ studies. While there is evidence of the dominant mechanisms that contributed to edge retraction, the role of other mechanisms that may have contributed to retraction has largely been unaccounted for. Additionally, the order in which the recognized mechanisms have taken place is also not clear. An in-situ study of Au/Ni bilayer films will allow the observation of edge retraction and agglomeration as it is occurring in the film. This study can be conducted in the ThermoFisher ESEM, which has video recording capabilities and a heating stage on which any chosen sample can be secured. There will be fundamental differences between this study and previous studies, such as instead of undergoing rapid thermal annealing, the sample will be heated and cooled gradually, revealing the effect that heating method has on long-range edge retraction specifically. Real-time observation of long-range edge retraction occurring will also reveal other contributing mechanisms and why certain mechanisms are dominant in some regions as opposed to others.

7.3 Additional characterization methods

The primary characterization methods employed in this study were SEM and EDX as they provided information about the morphology and chemical composition of the films, respectively. While this information was sufficient for the purposes of this study, employing other characterization methods can offer additional information. Transmission electron microscopy (TEM), for instance, can be utilized to conduct a cross-sectional study of the P5 region and collect information about the cross-sectional morphology of the region and the size, curvature, and contact angle of the rim to determine if a pinch-off event is indeed occurring in the region. A cross-sectional study of a sequence B sample prior to annealing would also definitively determine the existence of a native NiO_x layer.

8. References

1. W.D. Kaplan, D. Chatain, P. Wynblatt, W.C. Carter, A review of wetting versus adsorption, complexions, and related phenomena: the rosetta stone of wetting, J. Mater. Sci. 48 (2013) 5681e5717.
2. Cheynis, F., Bussmann, E., Leroy, F., Passanante, T., and Muller, P. Dewetting dynamics of Si-on-insulator thin films. Physical Review B 84, 24 (2011), 245439.
3. Thompson, C. V. Solid-State Dewetting of Thin Films. Annual Review of Materials Research 42, 1 (2012), 399–434.
4. Ye, J., and Thompson, C. V. Regular pattern formation through the retraction and pinch-off of edges during solid-state dewetting of patterned single crystal films. Physical Review B 82, 19 (2010), 193408.
5. Rabkin, E., Amram, D., and Alster, E. Solid state dewetting and stress relaxation in a thin single crystalline Ni film on sapphire. Acta Materialia 74, C (2014), 30–38.
6. Nichols, F. A., and Mullins, W. Surface- (Interface-) and Volume-Diffusion Contributions to Morphological Changes Driven by Capillarity. Transactions of the Metallurgical Society of AIME 233 (1965), 1840–1848.
7. Zucker, Rachel. (2015). Capillary-driven shape evolution in solid-state micro- and nano-scale systems.
8. Srolovitz, D., and Safran, S. Capillary instabilities in thin films. II. Kinetics. Journal of Applied Physics 60, 1 (1986), 255–260.
9. Wong, H., Voorhees, P., Miksis, M., and Davis, S. Periodic mass shedding of a

retracting solid film step. Acta Materialia 48, 8 (2000), 1719–1728.

10. Xi Cen, Xinming Zhang, Andrew M. Thron, Klaus van Benthem, Agglomeration and long-range edge retraction for Au/Ni bilayer films during thermal annealing, Acta Materialia, Volume 119, 2016 167-176.
11. G.H. Kim, R.V. Zucker, J. Ye, W.C. Carter, C.V. Thompson, Quantitative analysis of anisotropic edge retraction by solid-state dewetting of thin single crystal films, J. Appl. Phys. 113 (2013) 043512.
12. Sumiya T, Miura T, Fujinuma H, Tanaka S-i. Schottky barrier inhomogeneity at Au/Si (111) interfaces investigated using ultrahigh-vacuum ballistic electron emission microscopy. *Applied Surface Science* **117-118** (1997) 329-33.
13. Maier SA, Brongersma ML, Kik PG, Meltzer S, Requicha AAG, Atwater HA. Plasmonics - A route to nanoscale optical devices. *Advanced Materials* **13** (2001) 1501-+
14. Sahaym U, Norton MG. Advances in the application of nanotechnology in enabling a 'hydrogen economy'. *Journal of Materials Science* **43** (2008) 5395-429
15. Wagner RS, Ellis WC. Vapor-Liquid-Solid mechanisms of Single Crystal Growth. *Appl Phys Lett* **4** (1964) 89-&
16. Campbell CT. The active site in nanoparticle Au catalysis. *Science* **306** (2004) 234-5
17. Hannon JB, Kodambaka S, Ross FM, Tromp RM. The influence of the surface migration of Au on the growth of Si nanowires. *Nature* **440** (2006) 69-71
18. Shpyrko OG, Streitel R, Balagurusamy VSK, Grigoriev AY, Deutsch M, Ocko BM, et al. Surface crystallization in a liquid Au-Si alloy. *Science* **313** (2006) 77-80

D-3

19. Kodambaka S, Tersoff J, Reuter MC, Ross FM. Germanium nanowire growth below the eutectic temperature. *Science* **316** (2007) 729-32

20. Melechko AV, Merkulov VI, McKnight TE, Guillorn MA, Klein KL, Lowndes DH, et al. Vertically aligned carbon nanofibers and related structures: Controlled synthesis and directed assembly. *Journal of Applied Physics* **97** (2005) 39

21. Terrones M, Terrones H. The carbon nanocosmos: novel materials for the twenty-first century. *Philos Trans R Soc Lond Ser A-Math Phys Eng Sci* **361** (2003) 2789-806

22. Ajayan PM, Zhou OZ. Applications of carbon nanotubes. Carbon Nanotubes. Berlin: Springer-Verlag Berlin; 2001. p. 391-425.

23. C. Manuela Müller, R. Spolenak, Dewetting of Au and Au-Pt alloy films: a dewetting zone model, J. Appl. Phys. 113 (2013) 094301.

24. J. Petersen, S.G. Mayr, Dewetting of Ni and Ni-Ag solid thin films and formation of nanowires on ripple patterned substrates, J. Appl. Phys. 103 (2008) 023520.

25. Y. Kwon, N.H. Kim, G.P. Choi, W.S. Lee, Y.J. Seo, J.S. Park, Structural and surface properties of Ni-Cr thin films prepared by DC magnetron sputtering under variation of annealing conditions, Microelectron. Eng. 82 (2005) 314e320.

26. S. Yadavali, H. Krishna, R. Kalyanaraman, Morphology transitions in bilayer spinodal dewetting systems, Phys. Rev. B 85 (2012) 235446.

27. D. Amram, L. Klinger, E. Rabkin, Anisotropic hole growth during solid-state dewetting of single-crystal Au-Fe thin films, Acta Mater. 60 (2012) 3047e3056.

28. M. Perzanowski, Y. Zabila, J. Morgiel, A. Polit, M. Krupinski, A. Dobrowolska,

M. Marszalek, AFM, XRD and HRTEM studies of annealed Fe-Pd thin films, Acta Phys. Pol. A 117 (2010) 423e426.

29. P. Krishnakumar, Wetting and Spreading Phenomena, Physics 563 Phase Transitions and the Renormalization Group (University of Illinois at Urbana-Champaign, Champaign, IL), (2010), p. 1–12.

30. J.W. Cahn, J.E. Hilliard, Free energy of a nonuniform system, 1. Interfacial free energy, J. Chem. Phys. 28 (1958) 258e267.

31. W.W. Mullins, Theory of thermal grooving, J. Appl. Phys. 28 (1957) 333e339.

32. D.J. Srolovitz, S.A. Safran, Capillary instabilities in thin-films 2. Kinetics, J. Appl. Phys. 60 (1986) 255e260.

33. R.V. Zucker, G.H. Kim, W.C. Carter, C.V. Thompson, A model for solid-state dewetting of a fully-faceted thin film, Cr Phys. 14 (2013) 564e577.

34. E. Shaffir, I. Riess, W.D. Kaplan, The mechanism of initial de-wetting and detachment of thin Au films on YSZ, Acta Mater. 57 (2009) 248e256.

35. A.M. Thron, P. Greene, K. Liu, K. van Benthem, In-situ observation of equilibrium transitions in Ni films; agglomeration and impurity effects, Ultramicroscopy 137 (2014) 55e65.

36. P.R. Gadkari, A.P. Warren, R.M. Todi, R.V. Petrova, K.R. Coffey, Comparison of the agglomeration behavior of thin metallic films on SiO2, J. Vac. Sci. Technol. A 23 (2005) 1152e1161.

37. Carter, W., Roosen, A., Cahn, J., and Taylor, J. Shape evolution by surface diffusion and surface attachment limited kinetics on completely faceted surfaces. Acta

metallurgica et materialia 43, 12 (1995), 4309–4323.

38. Brandon, R., and Bradshaw, F. J. The mobility of the surface atoms of copper and silver evaporated deposits. Technical Report 66095 Royal Aircraft Establishment (1966).

39. Herz, Andreas & Wang, Dong & Schaaf, Peter. (2014). Dewetting of Au/Ni bilayer films on prepatterned substrates and the formation of arrays of supersaturated Au-Ni nanoparticles. Journal of Vacuum Science & Technology B: Microelectronics and Nanometer Structures. 32. 021802-021802. 10.1116/1.4863320.

40. J.A. Rodriguez, J.C. Hanson, A.I. Frenkel, J.Y. Kim, and M. Perez, J. Am. Role of Oxygen Vacancies in the Reduction of Nickel Oxide by Hydrogen. Chem. Soc.,124, 346 (2002).

41. Jeangros, Q., Hansen, T., Wagner, J., Damsgaard, C., Dunin-Borkowski, R., Hébert, C., Van herle, J. and Hessler-Wyser, A., 2012. Reduction of nickel oxide particles by hydrogen studied in an environmental TEM. *Journal of Materials Science*, 48(7), pp.2893-2907.

42. Hossain MM, De Lasa HI (2007) AIChE J 53(7):1817 16.

43. Jankovic B, Adnadevic B, Mentus S (2008) Chem Eng Sci 63(3):567 17.

44. Erri P, Varma A (2009) Ind Eng Chem Res 48(1):4

45. S. Bokstein, H.D. Bröse, L.I. Trusov, T.P. Khvostantseva. Diffusion in nanocrystalline nickel, Nanostructured Materials, Volume 6, Issues 5–8, 1995, Pages 873-876, ISSN 0965-9773.

46. Abdul-Lettif, A., 2003. Grain boundary diffusion coefficients in gold-nickel thin films. *Surface and Interface Analysis*, 35(5), pp.429-431.

47. Abdul-Lettif, A., 2004. Determination of diffusion coefficients in Au/Ni thin films by Auger electron spectroscopy. *physica status solidi (a)*, 201(9), pp.2063-2066.

48. Winzer, A., 1979. On the Quantum Theoretical Calculation of Activation Energies for the Self-Diffusion of Single Atoms and the Diffusion of Adatoms on Metal Surfaces (I). *Kristall und Technik*, 14(7), pp.857-876.

49. Argibay, N., Brumbach, M., Dugger, M. and Kotula, P., 2013. Grain boundary diffusivity of Ni in Au thin films and the associated degradation in electrical contact resistance due to surface oxide film formation. *Journal of Applied Physics*, 113(11), p.114906.

50. T. Nenadović, B. Perović, M. Adamov, B. Meckel. Diffusion in Au-Ni thin films. Thin Solid Films. Volume 25, Issue 2. 1975. Pages 515-524. ISSN 0040-6090.

51. S. M. Makin et al 1957 Proc. Phys. Soc. B 70 545.

52. J. R. MacEwan, J. U. MacEwan, and L. Yaffe. SELF-DIFFUSION IN POLYCRYSTALLINE NICKEL. *Canadian Journal of Chemistry*. **37**(10): 1623-1628.

53. Gupta, D., 1973. Grain-boundary self-diffusion in Au by Ar sputtering technique. *Journal of Applied Physics*, 44(10), pp.4455-4458.

54. Seeger, A. and Mehrer, H., 1968. Interpretation of Self-Diffusion and Vacancy Properties in Gold. *Physica Status Solidi (b)*, 29(1), pp.231-243.

55. T.G.M. van den Belt, J.H.W. de Wit. The diffusion of platinum and gold in nickel measured by Rutherford backscattering spectrometry. Thin Solid Films. Volume 109, Issue 1. 1983. Pages 1-10. ISSN 0040-6090.

56. Xi Cen, Andrew M. Thron, Klaus van Benthem. In-situ study of the dewetting behavior of Au/Ni bilayer films supported by a SiO2/Si substrate. Acta Materialia. Volume 140. 2017. Pages 149-156. ISSN 1359-6454.

57. Melmed, A., 1967. Surface Self-Diffusion of Nickel and Platinum. *Journal of Applied Physics*, 38(4), pp.1885-1892.

58. Manuela Müller, C. and Spolenak, R., 2013. Dewetting of Au and AuPt alloy films: A dewetting zone model. *Journal of Applied Physics*, 113(9), p.094301.

59. Xi Cen, Andrew M. Thron, Klaus van Benthem. In-situ study of the dewetting behavior of Au/Ni bilayer films supported by a SiO2/Si substrate. Acta Materialia. Volume 140. 2017. Pages 149-156. ISSN 1359-6454.

60. Harris Wong, P.W. Voorhees, M.J. Miksis, S.H. Davis. Periodic mass shedding of a retracting solid film step. Acta Materialia. Volume 48, Issue 8. 2000. Pages 1719-1728. ISSN 1359-6454.

61. Andreas Herz, Felix Theska, Diana Rossberg, Thomas Kups, Dong Wang, Peter Schaaf. Solid-state dewetting of Au–Ni bi-layer films mediated through individual layer thickness and stacking sequence. Applied Surface Science. Volume 444. 2018. Pages 505-510. ISSN 0169-433.

62. Herz, A., Wang, D., Kups, T. and Schaaf, P., 2014. Solid-state dewetting of Au/Ni bilayers: The effect of alloying on morphology evolution. *Journal of Applied Physics*, 116(4), p.044307.

Permission from publisher for reprinted material:

Dear Bhagyashree,

Sorry for our delay getting back to you about this.

The MIT Libraries Permissions Policy applies to MIT theses and grants permission to use figures in scientific works when the copyright is held by MIT. The title page of this thesis indicates that MIT is the copyright holder, so unless there is other information associated with the specific figure (if it was reprinted from somewhere else, for example, which would generally be indicated in the caption), you can rely on the policy and use that page as documentation.

If a more specific permission statement is helpful, please use this email as documentation of MIT's permission:

In response to your 2/18/21 inquiry, the copyright notice corresponding to "Capillary-driven shape evolution in solid-state micro- and nano-scale systems" by Rachel V. Zucker, 2015, attributes ownership to the Massachusetts Institute of Technology ("MIT"). Accordingly, MIT hereby grants permission to include figures 4-2 and 5-2 in your master's thesis, provided that any such use includes appropriate citation. This authorization to use the copyrighted material also applies to any future editions, revisions, or translations (in whatever language published) and to mechanical and electronic storage on any carrier.

Best regards,

Katie

Katie Zimmerman, JD, MLIS (pronouns: she/her)

Director, Copyright Strategy

MIT Libraries